İSTANBUL TECHNICAL UNIVERSITY ★ INSTITUTE OF SCIENCE AND TECHNOLOGY

CHARACTERIZATION OF Mo-N-Ag NANOCOMPOSITE COATINGS PRODUCED by MAGNETRON SPUTTERING

M.Sc. Thesis by

Tuncay TURUTOĞLU, B.Sc.

(706011006)

Date of submission : 18 July 2003
Date of defence examination: 29 July 2003

Supervisor (Chairman): Prof. Dr. Mustafa ÜRGEN

Members of the Examining Committee: Prof. Dr. Ali Fuat ÇAKIR

Prof. Dr. Mehmet DEMİRKOL

JULY 2003

ACKNOWLEDGMENTS

The author would like to appreciate to his advisor, Prof. Dr. Mustafa ÜRGEN, for his constant support, encouragement, and guidance throughout this study.

The author is grateful to Prof. Dr. Ali Fuat ÇAKIR for their helpful criticism and review.

The author is also grateful to Erdem ARPAT, Şakir Murat TELLİ, Bahadır KEPENEK and Ebru Devrim ŞAM for their invaluable discussions and helps with this project.

The author is grateful for the help of Ahmet ÖZTÜRK for preparation of coatings.

The author thanks his parents and sister for their continuous love, sacrifice and support through all the years.

July, 2003 Tuncay TURUTOĞLU

TABLE OF CONTENTS

ACKNOWLEDGEMENT ii
TABLE OF CONTENTS iii
ABBREVIATIONS vi
LIST OF TABLES vii
LIST OF FIGURES viii
LIST OF SYMBOLS x
ÖZET xi
SUMMARY xiii

1. INTRODUCTION 1

2. HARD AND SUPERHARD NANOCOMPOSITE COATINGS 3
2.1. Superlattice Coatings 6
2.2. Nanocomposite Coatings 8
2.2.1. Increase of Hardness and Toughness in Nanocomposite Coatings 12
2.2.1.1. Hall-Petch Effect 13
2.2.1.2. Griffith Theory 16
2.2.1.3. Koehler Theory 17

3. MAGNETRON SPUTTERING 18
3.1. Types of Magnetron Sputtering 19
3.1.1. Conventional Magnetron Sputtering 19
3.1.2. Unbalanced Magnetron Sputtering 20
3.1.3. Closed-Field Unbalanced Magnetron Sputtering 22
3.1.4. Pulsed Magnetron Sputtering 22
3.2. Control of Microstructure in Magnetron Sputtering 25
3.2.1. Ion Bombardment of Growing Film 25
3.2.2. Mixing Effect 27
3.3. Structure Zone Models 27
3.1.1. Zone I 29
3.1.2. Zone T 30
3.1.3. Zone II 31
3.1.4. Zone III 31

4. MOLYBDENUM NITRIDE AND SILVER 33
4.1. Molybdenum Nitride 33
4.1.1. Interstitial Nitrides 33
4.1.2. Molybdenum Nitride 35

4.1.3. Applications of Molybdenum Nitride 36
4.1.4. Preparation Methods 38
4.2. Silver 38
4.3. Molybdenum-Silver System 40

5. FRICTION AND WEAR **41**
5.1. Definition 41
5.2. Friction 42
5.3. Sliding Wear 42
5.3.1. Abrasion 43
5.3.2. Adhesion 44

6. FRETTING WEAR **45**
6.1. Fretting Wear 45
6.1.1. Fretting Wear in Mechanical Components 46
6.1.2. Molybdenum Nitride 47
6.1.2.1. Amplitude of Slip 47
6.1.2.2. Normal Load 49
6.1.2.3. Frequency 50
6.1.2.3. Evironmental Effects 50
6.2. Reciprocating Sliding Wear 50

7. EXPERIMENTAL PROCEDURE **52**
7.1. Substrate Preparation 52
7.2. Sputter Deposition 52
7.3. Characterization 53
7.3.1. X-Ray Diffraction Analysis 53
7.3.2. Energy Dispersive Spectrometry (EDS) Analysis 54
7.3.3. Thickness Measurements 54
7.3.4. Hardness Measurements 55
7.3.5. Roughness Measurements 56
7.3.6. Microstructure Investigations 56
7.3.7. Adhesion Properties 56
7.3.8. Wear Properties 56

8. RESULTS **58**
8.1. Crystal Structures 58
8.2. Energy Dispersive Spectrometry (EDS) Analysis 61
8.3. Thickness Measurement 62
8.4. Hardness Measurements 62
8.5. Roughness Measurements 63
8.6. Microstructure Investigations 63
8.7. Adhesion Properties 65
8.8. Wear Properties 66

9. DISCUSSION 69

10. CONCLUSIONS 73

REFERENCES 75

RESUME 80

ABBREVIATIONS

D.C.	: Direct Current
PVD	: Physical Vapor Deposition
FWHM	: Full Width at Half Maximum
HCP	: Hexagonal Close Packed
IBAD	: Ion Beam Assisted Deposition
JCPDS	: Joint Committee on Powder Diffraction Standards
CVD	: Chemical Vapor Deposition
R.F.	: Radio Frequency
HSS	: High Speed Steel
FCC	: Face Centered Cubic
EDS	: Energy Dispersive Spectrometry

LIST OF TABLES

		Page
Table 2.1.	Important steps in development of hard coatings	4
Table 4.1.	Nitrogen/Metal atomic radii ratio of interstitial nitrides	35
Table 4.2.	The atomic radius ratio of nitrogen atom to metal atoms	36
Table 7.1.	Parameters of fretting wear experiments	57
Table 7.2.	Chemical composition and mechanical properties of M50 tool steel balls	57
Table 8.1.	JCPDS card of γ-Mo_2N	60
Table 8.2.	JCPDS card of Ag	60
Table 8.3.	Lattice constants and grain sizes of γ-Mo_2N and γ-Mo_2N-Ag thin films	61
Table 8.4.	EDS analysis of γ-Mo_2N and γ-Mo_2N-Ag thin films	61
Table 8.5.	Thickness of γ-Mo_2N and γ-Mo_2N-Ag thin films	62
Table 8.6.	Hardness of γ-Mo_2N and γ-Mo_2N-Ag thin films	63
Table 8.7.	Surface roughness of specimens before and after deposition	63
Table 8.8.	Wear volumes of M50 tool steel balls and width of wear scars on γ-Mo_2N and γ-Mo_2N-Ag coatings	68

LIST OF FIGURES

		Page
Figure 2.1	: Schematic representation of a nanocomposite coating material.....	12
Figure 2.2	: Grain size strengthening.....	16
Figure 3.1	: Schematic representation of the plasma confinement observed in conventional and unbalanced magnetrons.....	21
Figure 3.2	: Dual unbalanced magnetron configurations.....	22
Figure 3.3	: Schematic diagram of basic particles and potentials in the low-pressure discharge.....	26
Figure 3.4	: Ideal (a) and real structure zone models of low (b), medium (c), and high (d) impurity concentrations.....	29
Figure 4.1	: Phase diagram of Mo-N system.....	37
Figure 4.2	: Crystal structure of γ-Mo_2N.....	37
Figure 4.3	: Phase diagram of Ag-Mo system.....	40
Figure 6.1	: Locations (indicated by F) prone to fretting in an aluminum-steel riveted joint.....	46
Figure 6.2	: Partial slip for a ball in contact with a flat and subjected to a tangential force.....	48
Figure 6.3	: Plot of normal load versus critical amplitude as a function normal slip for a crossed steel cylinder arrangement.....	48
Figure 6.4	: Plot of specific wear rate versus amplitude of slip.....	49
Figure 6.5	: Plot of wear versus frequency of fretting vibration.....	50
Figure 6.6	: The variation of fretting wear with amplitude of slip Δ for a wide range of steel.....	51
Figure 7.1	: (a) Schematic representation of calotest (b) optical microscope image of wear crater.....	55
Figure 8.1	: XRD spectra of γ-Mo_2N and γ-Mo_2N-Ag thin films.....	59
Figure 8.2	: Shifts in diffraction peaks of γ-Mo_2N and γ-Mo_2N-Ag coatings...	59
Figure 8.3	: SEM surface morphologies of as-deposited γ-Mo_2N and γ-Mo_2N-Ag thin films with different silver contents (a) γ-Mo_2N (b) γ-Mo_2N-Ag with 1% silver content (c) γ-Mo_2N-Ag 10% silver content.....	64
Figure 8.4	: SEM cross sections of as-deposited γ-Mo_2N and γ-Mo_2N-Ag thin films with different silver contents (a) γ-Mo_2N (b) γ-Mo_2N-Ag with 1% silver content (c) γ-Mo_2N-Ag 10% silver content.....	64
Figure 8.5	: Rockwell C indentations of as-deposited γ-Mo_2N and γ-Mo_2N-Ag coatings with different silver contents (a) and (d) γ-Mo_2N (b) and (e) γ-Mo_2N-Ag with 1% silver content (c) and (f) γ-Mo_2N-Ag with 10% silver content.....	65
Figure 8.6	: Friction coefficient-distance graphs of γ-Mo_2N and γ-Mo_2N-Ag coatings.....	66

Figure 8.7 : Scanning electron microscope images of wear scars on M50 balls and γ-Mo_2N and γ-Mo_2N-Ag coatings. (a) and (b) γ-Mo_2N coating, (c) and (d) γ-Mo_2N-Ag coating with 1 at % silver content, (e) and (g) γ-Mo_2N-Ag coating with 6 at % silver content and (g) and (h) γ-Mo_2N-Ag coating with 10 at % silver content..... 67

LIST OF SYMBOLS

v	: Poisson ratio
λ	: Wavelength of X-ray
θ	: Diffraction angle of X-ray
d	: Distance between crystal planes
h, k, l	: Indices of crystal planes
Ra	: Average roughness value
T_m	: Melting temperature of substrate
T_s	: Deposition temperature of substrate
Λ	: Superlattice period

MANYETİK SIÇRATMA YÖNTEMİ İLE ÜRETİLMİŞ Mo-N-Ag NANOKOMPOZİT KAPLAMALARIN KARAKTERİZASYONU

ÖZET

Sert kaplamalar malzemelerin korunması amacı ile uzun yıllardır başarı ile kullanılmaktadır. Sertliklerine göre kaplamaları iki ana sınıfa ayırmak mümkündür:

1. Sertlikleri 40 GPa'dan düşük olan sert kaplamalar.
2. Sertlikleri 40 GPa'dan yüksek olan çok sert kaplamalar.

Günümüzde çok sert kaplamaların üretilmesi için süperlatis ve nanokompozit kaplamalar gibi birçok yaklaşım geliştirilmiştir. Nanokompozit ince filmler sahip oldukları çok küçük tane boyutu nedeni ile çok iyi mekanik özelliklere sahiptir ve bu birçok uygulama için oldukça umut vericidir.

Yüksek sertlik değerine sahip nanokompozit ince filmler sadece iki sert fazdan değil biri sert diğeri yumuşak iki fazdan da meydana gelebilmektedir. İkinci yaklaşım sert/yumuşak faz kombinasyonunun sert/sert faz kombinasyonuna göre çok daha fazla olması avantajına sahiptir.

Bu çalışmada sert/yumuşak faz kombinasyonundan oluşan Mo-N-Ag nanokompozit kaplamalarının mekanik ve mikroyapısal özelliklerinin kaplama içerisindeki gümüş içeriği ile nasıl değiştiği incelenmiştir. γ-Mo_2N kaplamalar TiN, CrN ve ZrN gibi birçok nitrürden daha yüksek sertlik değerine sahiptir. Nanokompozit kaplamaların sertlikleri, nitrürleri ile karşılaştırıldığında çok daha yüksek olduğu için γ-Mo_2N kaplamalar nanokompozit kaplamarın üretilmesi çalışmaları için ilk alternatif olmaktadır.

Kaplama İşlemi:

Kaplamaların yapıldığı altlık malzemesi olarak yüksek hız çeliği (YHÇ) kullanılmıştır. Altlıklar yüzey pürüzlülük değerleri Ra=0.06 olana kadar parlatılmışlardır. Parlatma işleminden sonra altlıklar alkali çözelti içerisinde ultrasonik olarak temizlenmiş ve hemen propanol çözeltisi içerisinde kurutulmuştur.

Kaplamadan önce bütün altlıklar Mo iyonları ile -600, -800 ve -1000 V bias voltajı altında 2'şer dakika bombardıman edilerek kaplama sıcaklığına kadar arc PVD katodu ile ısıtılmıştır. Kaplamanın yapılabilmesi için numuneler magnetronun önüne getirilmiştir. Magnetron güç kaynağına Mo hedefi buharlaştırmak için 500 W güç uygulanmıştır. Kaplama süresi 20 dakikadır. Kaplamaların gümüş içerikleri molibden hedef üzerindeki gümüş parçalarının çapları değiştirilerek ayarlanmıştır.

Kaplamaların Yapıları ve Morfolojileri:

XRD incelmeleri Cu-Kα radyasyonu kullanan difraktometrenin ince film modunda gerçekleştirilmiştir. Kaplamaların tane boyutları Sherrer formülü kullanılarak hesaplanmıştır.

XRD incelemeleri göstermiştir ki kaplamanın gümüş içeriğinin artması ile

1. XRD pikleri genişlemiş fakat tane boyutlarında önemli bir azlama olmamıştır. Bu γ-Mo_2Ntane boyutların zaten oldukça küçük olmasına bağlanabilir.
2. γ-Mo_2N kaplamalarda basma kuvvetlerin varlığını gösteren negatif yöndeki kayma kaplama içerisine giren gümüş miktarının artması ile ortadan kalkmaktadır. Bu kaplamadaki iç gerilmelerin ortadan kalktığını göstermektedir.
3. γ-Mo_2N kaplamalarda belirli bir yönlenme yoktur ve mevcut olan az miktardaki yönlenme gümüş içeriğinin artması ile tamamen ortadan kalkmaktadır.

XRD difraksiyon paternlerinde hiç bir gümüş pikine rastlamamıştır. Bu gümüşün yapıda amorf halde ya da nanokristalin olarak bulunduğunu göstermektedir.

Taramalı elektron mikroskobunda yapılan kırık yüzey çalışmalarında γ-Mo_2N fazının yoğun ve kolonsal bir yapıya sahip olduğu görülmüştür. γ-Mo_2N kaplamları Zone II yapısına sahiptirler. Bütün kaplamalarda gümüş içeriğinin artması ile yapı daha yoğun bir hale gelmiştir. Yüksek gümüş içeriklerinde kolonsallık ortadan kalkmakta ve kristalin yapı belirsizleşmeye başlamaktadır.

Kaplamaların Sertliği:

Sertlik ölçümleri, 0.2 mN yük hassasiyetine ve 0.01 nm derinlik hassasiyetine sahip Fischer Ultra Mikrosertlik cihazında yapılmıştır. Yük, 0.2 mN'luk adımlar halinde sertlik ucunun kaplama kalınlığının onda biri derinliğe girecek şekilde 100 mN olarak uygulanmıştır. Her bir ölçüm 25 defa tekrarlanmış ve ölçümlerin ortalaması alınmıştır. En yüksek sertlik değeri 3430 kg mm^{-2} (33 GPa) ile %1 gümüş içeriğine sahip kaplamaya aittir. Saf γ-Mo_2N kaplaması ise 2860.7±15.0 Hv en düşük sertlik değerine sahiptir.

Kaplamaların Yapışma Özellikleri:

Mo-N-Ag sistemi kaplamaların yapışma özelliklerini incelemek amacı ile elmas Rc ucu ile 1500 N yük uygulanarak kaplanmış numuneler üzeründe Rockwell C izleri oluşturulmuştur. Oluşan izler optik mikroskopta incelenerek kaplamanın taban malzemeye iyi yapışıp yapışmadığına karar verilmiştir. Bazı kaplamalarda yüzeyden kalkma gözlenmiştir. 1% gümüş içeriğine sahip olan kaplamanın yüzeyden kalkmalar gözlenmiş ancak kaplama taban malzemeden ayrılmamıştır.

Kaplamaların Aşınma Özellikleri:

Kazımalı aşınma testleri γ-Mo_2N ve γ-Mo_2N-Ag kaplamalar üzerinde 50 Hz frekans, 1 mm genlik, 5 N yük, % 40 bağıl nem ve 28 °C sıcaklık altında 60 dakika süre ile gerçekleştirilmiştir. Karşıt malzeme olarak M50 takım çeliği bilye kullanılmıştır. Kaplamalarda her hangi bir aşınma derinliği ölçülememiştir. Ancak toplardaki aşınma oranları $5.61x10^{-3}$ ile 11.8 $x10^{-3}$ mm^3 arasında değişmektedir. En yüksek aşınma % at 1 gümüş içeren kaplamanın karşıt malzemesi olan topta görülmüştür.

Kaplamaların sürtünme katsayıları 0.78 ile 0.94 arasında değişmektedir ve belirli bir eğilim söz konusu değildir.

CHARACTERIZATION OF Mo-N-Ag NANOCOMPOSITE COATINGS PRODUCED BY MAGNETRON SPUTTERING

SUMMARY

Hard coatings have been successfully used for protection of materials. As to the hardness, the coatings are usually divided into two groups:

1. Hard coatings having a hardness <40 GPa.
2. Superhard coatings having a hardness >40 GPa.

There are some new approaches to produce superhard coatings such as superlattice and nanocomposite coatings. Nanocomposite thin films are very promising materials which exhibit very good mechanical properties due to their very small grain sizes.

Nanocomposite thin films with high hardness values not only can be composed of two hard phases but also can be composed of one hard and one soft phase. The second approach has the advantage of being applied in extended combinations when compared to hard-hard nanocomposite thin films due to their limited production opportunities.

In this study the effect of silver content on the mechanical and structural properties of a hard-soft nanocomposite coating system composed of Mo-N-Ag is studied. γ-Mo_2N coatings have very high hardness compared to most of the nitride coatings, such as TiN, CrN and ZrN. Since the hardness is increased dramatically in nanocomposites when compared to their nitrides, γ-Mo_2N coating systems become first candidate to investigate production of nanocomposite coatings from these systems.

Coating Process:

High speed steel (HSS) specimens are used as a substrate materials in the experiments. All substrates are subjected to a polishing procedure until average surface roughness value, Ra=0.06 μm is achieved. After polishing, substrates are ultrasonically cleaned in alkaline bath and immediately dried in propanol.

Before the coating, the substrates were heated by cathodic arc PVD up to deposition temperature by etching with molybdenum ions at -600, -800 and -1000 V bias each for 2 min. Samples were moved in front of the magnetron gun and deposition of coating occurred. Magnetron power supply power evaporating the Mo target was 500 W. The deposition time was about 30 minutes. Silver content in the coatings were controlled by changing of diameters of silver spots on Mo target.

Structure and Morphology of the Coatings:

The XRD investigations are made in thin film mode of the diffractometer (angle of incidence 1°) by using Cu-Kα radiation. The grain sizes of the coatings are calculated by Scherrer's equation.

The XRD investigations revealed that by the addition of silver to the coatings:

1. XRD peaks are broadened but grain sizes sligthly decreased. This can be attributed to the original small grain size of γ-Mo_2N coatings.
2. The negative shift in γ-Mo_2N coating which is an indication of compressive stress shifted back to its original position by the increase of silver content in the film. Thus indicating of stress reduction in the film.
3. No preffered orientation observed in γ-Mo_2N coating diminishes by the addition of silver in the film.

There is no silver peak is observed in XRD diffraction patterns shows that silver is in amorphous or nanocrystalline structure in the film structure.

In scanning electron microscopy analyses on fractured surfaces, a dense structure was observed with clear columnar structure has been observed in γ-Mo_2N phase. γ-Mo_2N coatings matched with Zone II structure. In all of the coatings an increase in silver content resulted in a dense structures. At high silver contents a featureless structure is observed on fracture cross sections of the films.

The Hardness of Coatings:

Hardness measurements were carried out on Fischer Ultra Microhardness Tester with load sensitivity of 0.2 mN and depth sensitivity of 0.01 nm. Load was applied in steps of 0.2 mN so that the Vickers pyramid indenter penetrates to tenth part of coating thickness. Each measurement was repeated at least 25 times for an average hardness value. The highest hardness was about 3430.7±25.4 Hv, which was measured on the γ-Mo_2N-Ag coating with 1% Ag content. The samples with pure γ-Mo_2N phase had the lowest hardness values of about 2860.7±15.0 Hv.

Adhesion Properties of Coatings:

In order to investigate the adhesion properties of Mo-N-Ag coatings, an indentation is formed by using diamond Rc indentor at normal load of 150 N. It is decided whether the adhesion of the coating to the substrate is sufficient or not by observation of the indentations with scanning electron microscope. Some of the coatings spalled out from the substrate after indentation. The delamination of the hardest coating containing 1% silver observed but there was still continious coating on the surface.

Wear Properties of Coatings:

Fretting test were conducted on γ-Mo_2N and γ-Mo_2N-Ag coatings under the conditions of frequency of 50 Hz, amplitude of slip of 1 mm, load of 5 N, 40 % relative humidity, temperature of 28 °C for 60 minutes. M50 tool steel balls were used as counterbody. Wear depth of coatings could not be measured. But, wear volumes of M50 tool steel balls changes between 5.61×10^{-3} and 11.8×10^{-3} mm^3. The maximum wear volume belonged to M50 tool steel ball which was counterbody of γ-Mo_2N-Ag coating with 1 at % Ag content.

Friction coefficients of γ-Mo_2N and γ-Mo_2N-Ag coatings changes between 0.78 and 0.93 and there was no tendency of friction coefficient observed.

1. INTRODUCTION

Developing technology and competition in industry requires the new materials which can resist hard working conditions when friction and wear occurs. The most effective way to produce the materials which have required properties is coating their surfaces with protective materials [1].

Nanocomposite coatings are very promising materials which exhibit very good mechanical properties due to their very small grain sizes [2]. Among the application areas tribological applications of nanocomposite coatings is a very important subject and significant research has been made on different systems [3, 4].

Nanocomposite coatings with high hardness values not only can be composed of two hard phases [5] but also can be composed of one hard and one soft phase [6]. In the second group of nanocomposite coatings, nanocrystallites of hard phase material embedded within a very thin amorphous matrix of soft phase material. Such nanocomposite coatings often have higher hardness values than for single phase material. Improvement of hardness and toughness values are caused by the strong hindering of the crack formation and propagation in the thin amorphous matrix between the nanocrystallites.

At present, it was shown that γ-Mo_2N coatings are very good candidates for tribological applications with their mechanical properties make them wear resistant material and used as hard phase in nanocomposite coatings [7, 8]. It is also known that Ag is used in wide range of tribological applications due to its lubricating properties and used as soft phase material in nanocomposite coatings [9-11]. Nanocomposite coating composed of γ-Mo_2N as hard phase material and Ag as soft phase material can show good tribological properties [12].

The amount of soft phase material in the nanocomposite coating coatings is an important parameter that affects the mechanical and structural properties. In this study, the effect of the Ag content in magnetron sputtered γ-Mo_2N-Ag

nanocomposite coatings on the mechanical and structural properties were investigated.

2. HARD AND SUPERHARD NANOCOMPOSITE COATINGS

Hard coatings have been successfully used for protection of materials and particularly to enhance the life of cutting tools since the 1970s. Both the technological process of their production and their properties, i.e. hardness, wear and oxidation resistance, however, are continuously being improved. Important milestones in the development of hard coatings are briefly summarized in Table 2.1. This table shows a clear effort to decrease the temperature T at which hard coating is formed and to improve the properties of hard coatings, particularly to increase the hardness and oxidation resistance. The oxidation resistance should be increased up to approximately 1000 °C because during high-speed machining the temperature of the tool tip can reach 1000 °C and the coating should be stable at such high temperatures.

As to the hardness, the coatings are usually divided into two groups:

1. Hard coatings having a hardness <40 GPa.
2. Superhard coatings having a hardness >40 GPa.

Compared to a large number of hard materials, there are only a few superhard materials, i.e. cubic boron nitride (c-BN), amorphous diamond-like carbon (DLC), amorphous carbon nitride (a-CN_x) and polycrystalline diamond. Moreover, these superhard materials are thermodynamically unstable. This is a serious disadvantage which strongly limits their utilization in some applications. For instance, the high chemical affinity of carbon to iron limits the applicability of diamond coated cutting tools to machining of aluminum, their alloys and wood only. Similar problems can be expected when the c-BN coating is used in cutting of steels due to the chemical dissolution of boron in iron. These problems stimulated intensive research in this field, and recently new superhard materials based on superlattice and nanocomposite structures were developed [3].

Table 2.1 Important steps in development of hard coatings [3]

Coating	Material	H (GPa)	Main characteristics
Single layer	TiN, TiC, Al_2O_3	21, 28, 21	CVD at T around 1000°C on cemented carbides
Single layer	TiN, TiC	21, 28	PVD at T 550°C on steel substrates
Multilayer	TiC/TiB_2		About 103 phase boundaries TiC/TiB_2
Single layer	c-BN	50	High chemical affinity of C to iron
Single layer	Diamond	90	Chemical dissolution of B in iron
Single layer	TiAlN		Oxidation resistance up to 800°C
Single layer	DLC	65	Amorphous phase
Single layer	CNx	50–60	Substoichiometric (x=0.2–0.35) turbostratic structure
Superlattice	TiN/VN, TiN/NbN, etc.	~50	Superlattice period 5–10 nm
Single layer	nc-MeN/a-nitride	~50	Superlattice period 5–10 nm
Single layer	nc-MeN/metal	~50	Nanocomposite
Single layer	$Ti_{0.4}Al_{0.6}N$	~32	Nanocomposite, oxidation resistance up to 950°C

Hardness measures a material's ability to resist deformation. The upper limit of hardness is determined by the rigidity of a material's crystal structure. There are three factors that contribute to the rigidity of a crystal structure:

1. Large coordination number (CN) of the atoms
2. High covalent character of bonds
3. Short interatomic distance of the structure, i.e., small atoms.

A high CN number allows atoms to be surrounded by a large number of neighbors, so each atom is supported by more bonds. A high degree of covalence increases the strength of these bonds, so each atom is held firm in its lattice position. Small atomic size makes bonds shorter so it improves the effectiveness of the support. The combined effect of these three factors is to concentrate the bond energy in a small volume, so a large stress is required to deform the crystal lattice. This stress measures the intrinsic hardness of the material.

The effect of CN on hardness is revealed by the contrast of hardness between diamond and graphite. Although these two phases are polymorphs of carbon and their bonds are both covalent, they differ in CN. Carbon atoms in diamond are in four-fold (tetrahedral or sp^3) coordination. These bonds are symmetrically distributed with a bond angle of 109°47'. As a result, the crystal lattice is supported in all directions. In contrast, carbon atoms in graphite are in three-fold (ternary or sp^2) coordination. These atoms do not have enough bonds to form a, three-dimensional network, so they form two-dimensional basal planes. These planes are held together by weak van der Waals bonds. As a result, graphite becomes one of the softest materials known.

The effect of bond covalence on hardness is depicted in the following example. Sodium chloride (rock salt) is very ionic, aluminum highly metallic, and grey tin (a-phase) entirely covalent. All of them have comparable bond lengths of about 2.80 A. The Knoop microhardness increases from sodium chloride (30 kg mm^{-2}), to aluminum (100 kg mm^{-2}), to grey tin (450 kg mm^{-2}). In this case, the covalent bonds have made grey tin hardest despite it having the fewest bonds per atom among the three phases (4 in grey tin compared with 6 in sodium chloride and 12 in aluminum).

The effect of atomic size on hardness is reflected in the hardness difference of Group IV elements. All a phases of C, Si, and Ge form the same diamond structure and their bonds are completely covalent. The different hardness among them is due to their different atomic sizes. Thus, hardness decreases with increasing atomic size, diamond being the hardest because carbon atoms are the smallest among these elements [13].

A high strength of materials is achieved by a combination of a high value of the bulk modulus and an appropriate microstructure. The bulk modulus B is related to the force constant of the interatomic bond, i.e. the second derivative of the bond energy, E:

$$\frac{d^2E}{da^2} \tag{2.1}$$

at a_o, a_o is the bond distance. Thus, a high bond energy and short bond distance are necessary for a high value of B. High bond energy means a high electron density

between the neighboring atoms, i.e. a covalent, nonpolar bond [4]. This is the physical basis of the theoretical approach of Cohen et al., who arrived at the conclusion that the hardness of C_3N_4, should almost reach that of diamond. However, the hardness of stoichiometry amorphous C_3N, films reaches only about 3000 kg mm^{-2} [14]. Whereas that of substoichiometric CN_x, X = 0.2-0.35, reaches 5000-6000 kg mm^{-2}. This result emphasizes the fact that the strength of materials is predominantly determined by the microstructure.

Indeed, the practically achievable strength of materials is two to three orders of magnitude lower than the theoretical one. It can be increased by various methods of strengthening such as precipitation and solution hardening, and smaller crystallite sizes [15].

However, the Hall-Petch relation, which governs the latter method of hardening, loses its validity and a softening is observed when the grain size D decreases below a critical dimension. This is the negative slope effect in the Hall-Petch relationship. There is no unique explanation of this phenomenon. Some researchers have presumed it to be due to creep, or to the retention of air cavities, while others speculated that it is due to recovery of ordering [16].

2.1. Superlattice Coatings

Multilayer coatings have been used for many years in applications such as optical, magnetic, electronic, corrosion protection, and tribological. For tribological applications, successful coatings generally exhibit high hardness and adhesion, as well as good oxidation resistance. Early multilayer coatings for cutting tool applications consisted of layers of TiN and TiCN, each of which was several microns thick. It was shown that these multilayer coatings could improve the life of the cutting tool beyond that of an individual coating of TiN or TiC. Other successful multilayer coatings for cutting tool applications are based on combinations of a nitride or carbide material and an oxide, such as TiN or TiC and Al_2O_3. The nitride/carbide layer provides strength and refines the grain size of the oxide, and the oxide layer provides chemical resistance to make this coating very useful in cutting applications. Individual layer thicknesses in these coatings are generally on the order of 0.5 μm, and the total coating thickness is 5-10 μm.

Over the past 10 years, a new class of multilayer materials has emerged that exhibit extremely high hardness, making them very attractive for tribological applications. Multilayer structures consisting of very thin (2-10 nm) layers of nitride materials were deposited by magnetron sputtering, and these coatings have hardness in excess of 5000 kg mm^{-2}. This hardness is comparable to that of cubic-BN and is second only to diamond. This special class of multilayer structures (sometimes called superlattice structures) has been the subject of many recent studies to determine the mechanisms that give rise to this high hardness. The bilayer period, Λ, was found to be the most important parameter of the coating, since the high hardness generally occurs in a narrow range of Λ of 5-10 nm. Several explanations have been proposed including, dislocation blocking by layer interfaces, Hall-Petch strengthening, strain effects at layer interfaces, and the supermodulus effect. Dislocation blocking occurs when the two layers of the multilayer have different shear modulus, and therefore different dislocation line energies. In this case, dislocations prefer to remain within the layer with the lower shear modulus. An additional stress is required to move the dislocation into the layer with the higher shear modulus compared to the stress required to move the dislocation in a homogeneous film with the lower shear modulus. The Hall-Petch effect, originally used to explain the increase in hardness with decreasing grain size in bulk polycrystalline metals, has also been used to explain the hardness enhancements in multilayer structures. Also, the effect of an alternating strain field due to the lattice mismatch between the layers has been studied, but this effect is believed to be small compared to dislocation line energy effects. Finally, early measurements on metallic multilayer structures showed large enhancements (~100%) of the elastic constants, a so-called supermodulus effect. Since the hardness is dependent on the elastic properties of a material, this has been used to explain the hardness enhancements. However, attempts to reproduce the results of these studies have shown only small variations in the elastic modulus (~10%), and it is generally believed that the original reports were due to the difficulty in accurately measuring the elastic properties of thin films [17].

2.2. Nanocomposite Coatings

The nanocomposite materials are composed of at least two or more phases which have grain sizes at nanometer scale. According to the size, d, of grains, materials can be divided into two groups:

1. Nanocomposites with $d \geq 100$ nm, which represent so called conventional materials.
2. Nanocomposites with $d < 100$ nm, which represent a new generation of materials.

The second group of materials exhibits new physical, functional and service properties. It is due to the fact that in the case when the size d of grains decreases to approximately 10 nm and less the number of atoms in a boundary region, which surrounds the grain, is comparable or even greater than that in the grain. This fact dramatically changes interaction between grains, for instance, hinders the generation of dislocations and prevents cracks propagation due to the grain boundary enhancement and suppression of grain boundary sliding and strongly decreases the macrostress generated in nanocomposite coatings when the grain size is <10 nm. Therefore, it is not surprising that nanocomposite coatings exhibit completely new properties [18].

The formation of nanocomposite structures is connected with a segregation of the one phase to grain boundaries of the second phase, and this effect is responsible for stopping of the grain growth [3]. The theoretical concept for the design of the superhard nanocrystalline composites is associated with the preparation of a composite material consisting of nanocrystallites embedded within a very thin amorphous matrix. Such multiphase materials often display higher hardness and toughness values than for single phase materials. The superhardness appears due to the strong hindering of the crack formation and propagation in the thin amorphous tissue between the crystallites [19].

A systematic investigation carried out on systems Zr-Cu–N and Ti-Al–N showed that superhard nanocomposite coatings can be composed not only of two hard phases as proposed by Veprek et al. but also in the case when only one phase is hard, e.g. a nc-ZrN/Cu nanocomposite. This means that there are two groups of superhard nanocomposite coatings:

1. nc-MeN/nitride (e.g. a-Si_3N_4, a-TiB_2, etc.);
2. nc-MeN/metal (e.g. Cu, Ni, Y, Ag, Co, etc.).

The hardness, H, of films of both groups can be continuously varied from low values of about 10 GPa to very high values, achieving up to 50–70 GPa. Moreover, it is worthwhile to note that the hardness of nanocomposite films is strongly correlated with their structure.

The structure of hard (<40 GPa) and superhard (>40 GPa) nanocomposite coatings is significantly different. A systematic investigation of the correlation between the hardness and structure in the Zr-Cu–N and Ti-Al–N nanocomposite films showed that

1. The hard films are characterized by many reflections from poly-oriented grains of both phases.
2. The superhard films are two-phase nanocomposites one phase of which has a nanocrystalline structure and the second is X-ray amorphous.
3. The maximum hardness is achieved only when all grains are oriented in the same direction and the size of grains has an optimum value of approximately tens of nanometers.

At present, no definite methodology exists on how to select the combination of elements to produce films with nanocrystalline and/or X-ray amorphous structure. Such films can be formed from nitrides of alloys composed of elements which exhibit a wide miscibility gap and contain one element forming hard nitride, for instance nitrides of binary alloys formed of immiscible elements such as Cu–Cr, Zr–Y, etc. or transition metal nitride/boride and nitride/carbide systems. A miscibility gap between intermetallics is also sufficient to produce hard nanocomposite coating, e.g. Zr-Cu–N film. There is also a possibility to produce the nanocomposite coating from nitrides of alloys whose elements form a solid solution, e.g. $Ti_{1-x}Al_xN$ film. This is enabled by the existence of a gap in the alloy composition x where the structure of the film is quasi-X-ray amorphous [3].

Till now, various different types of hard nanocomposite coating have been prepared:

1. nc-MeN/a-nitride, e.g. nc-MeN/a-Si_3N_4 (Me=Ti, W,V), nc-TiN/a-Si_3N_4
2. nc-MeN/nc-nitride, e.g. nc-TiN/nc-BN

3. nc-MeC/a-C, e.g. nc-TiC/DLC
4. nc-MeN/ metal, e.g. nc-ZrN/Cu, nc-(Ti, Al)/AlN, nc-CrN/Cu
5. nc-MeN or MeC/a-boron compounds, e.g. nc-Ti(B,O)/quasi-a-(TiB_2, TiB and B_2O_3), Ti–B–C;
6. nc-WC+nc-WS_2/DLC
7. nc-MeC/a-C+a-nitride, e.g. nc-Mo_2C/a-C+a-Mo_2N.

When the grain size decreases below about 10-20 nm, the strength and hardness decreases. This phenomenon is so called negative or reverse Hall–Petch relationship. The majority of researchers believe that this softening is associated with grain boundary sliding. Although the grain size, where the slope of the Hall–Petch plot changes the sign, depends on the given nanocrystalline system and, in a given system on the sample preparation, such as compactions, the fact, that the nanosoftening is found also for compact films sputter-deposited under vacuum underlines the believed universality of this phenomena. Recent computer simulations indicate that the reverse Hall–Petch effect is possible also in the absence of porosity in the grain boundaries, and that the grain boundary sliding can occur without any thermally activated process. The reason of the grain boundary sliding appears to be the reduction of the elastic modulus of the disordered grain boundary material.

The concept for the design of superhard materials therefore addresses the question of forming a strong interface between the segregated phases, each of them being also a strong material. If the grain boundary sliding is suppressed in this way, the reverse Hall–Petch effect is avoided and the strength and hardness will increase.

One possibility is a combination of a hard nanocrystalline material having a grain size of $\leq$10 nm with an amorphous one, the latter having a sufficient structural flexibility to form a strong interface. Alter- natively, one can choose two crystalline materials which show a sufficient commensurability (coherence, template effect, etc.) at the interface (see above). Dislocation multiplication source cannot operate in such small crystallites and - if ever formed - dislocations cannot pass the amorphous tissue under an applied stress. In the case of a nanocomposite consisting of two nanocrystalline materials with different elastic modulus the elastic mirror force will hinder the dislocation to pass the interface. Thus, such a material should display a brittle behavior [20].

The strength enhancement should be achieved in epitaxial heterostructures consisting of a few nanometer thin layers of two metals A and B with a high and low elastic modulus, respectively. The Frank-Read source for dislocation multiplication cannot operate in such thin layers. The dislocations will be formed only in metal B with the lower modulus. Upon applied stress they will be hindered to cross the B/A interface due to a repelling force of their image in A [21]. Figure 2.1(a) shows a schematic drawing of a nanocomposite consisting of two materials of different elastic properties, e.g. brittle nanocrystals of material A (nc-A) and an amorphous or quasi-amorphous matrix B (a-B). Due to limited grain volume and the consequent inability of Frank–Read dislocation sources to be operable in these systems, plastic deformation is assumed to be essentially limited. However, Shiotz et al. showed very recently that deformations of nanocrystalline metals are mainly due to small sliding events in the grain boundary phase [22]. Only occasionally, partial dislocations nucleated at a grain boundary may move through a grain leaving behind a stacking fault [see Figure 2.1(b)]. If not removed by a second partial dislocation it seems possible that these stacking faults act as crack nuclei if larger deformations occur [see Figure 2.1(c), case 1].

Extensive plastic deformation of the amorphous grain boundary phase with the assumed higher ductility may lead to crack nucleation by void coalescence and formation of pores [see Figure 2.1(b)]. The superhardness observed by various authors for e.g. nc-TiN/a-Si_3N_4 has been attributed to trapping of these cracks between the nanocrystals. Veprek et al. based their model for superhard nanocomposites on the Griffith theory of crack growth for ideal brittle materials with crack lengths on the order of a few nanometers. However, if the cohesive strength of the interface nc-A/a-B is not sufficient to withstand the local tensile stress at the crack tip, unstable crack propagation and debonding of the nanocrystals will result [see Figure 2.1(c), case 2] [23].

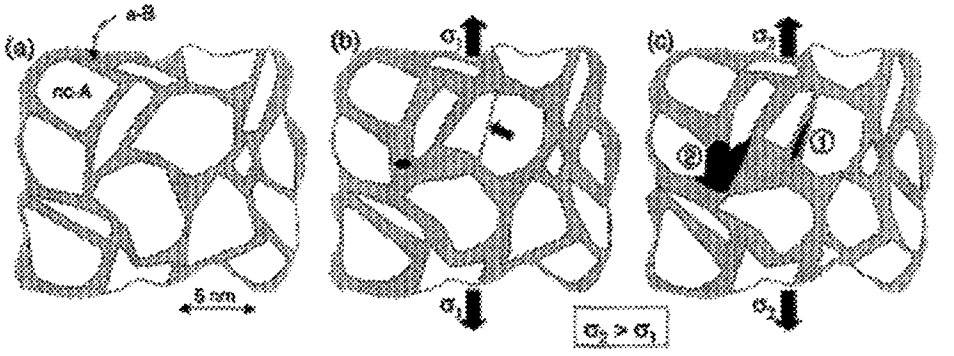

Figure 2.1 (a) Schematic representation of a nanocomposite coating material (nc-A, nanocrystalline phase A; a-B, amorphous phase B). (b) Grain boundary sliding leads to repositioning of the nanocrystals, formation of a stacking fault left behind by a partial dislocation (arrow) and a pore. (c) Crack nucleation at stacking fault 1, crack propagation and debonding of nanocrystals [23].

While Figure 2.1 may serve as a simplified schematic drawing of failure mechanisms in nanocomposite materials, it is assumed that multiple mechanisms are responsible for hardness and toughness optimization and that it is the synergism between these mechanisms that is most important. However, it has to be concluded that not only the nanoscale grain size, but also the interfacial arrangement and the interface strength play important roles in determining coating properties. To avoid unstable crack propagation, a well-defined interface of high cohesive strength is needed. Inferred from thermodynamics, this may be obtained for those compounds showing a wide miscibility gap in the solid state but a certain chemical affinity to each other to form high-strength grain boundaries [23].

2.2.1. Increase of Hardness and Toughness in Nanocomposite Coatings

When the crystallite size decreases below critical value softening is observed due to grain boundary sliding which is believed to be an intrinsic property of nanocrystalline material limiting their hardness. The grain boundary sliding and softening are caused by the large defect density in the grain boundaries which allows fast diffusion of the atoms and vacancies in the stress field mainly due to a kind of Coble diffusion [24, 25].

If however a binary system is used which shows a strong thermodynamically driven segregation (spinodal decomposition which is a special case of immiscibility where the formation of the two phases occurs congruently without activation due to infinitesimal small fluctuations) a nanocomposite is formed which has a strong interface.

Such situation is found for example in the nitride systems M_nN/Si_3N_4 (M = transition

metal which forms stable and hard nitride, Ti, V, Cr, W.) provided the activity of nitrogen is sufficiently high as found e.g. during plasma CVD or PVD in an intense discharge plasma at the substrate surface. Because the spinodal decomposition takes place without activation a nanocomposite is formed. In such systems there exists an optimum composition of the two phases at which the second phase percolates and a nanocomposite with about 3 nm small crystallites of the transition metal nitride imbedded within few nanometer thin tissue of amorphous Si_3N_4 is formed.

The temperature at which the thermodynamic force for the segregation decreases and the two (or more) phases become miscible determines the upper limit of the thermal stability of the nanocomposites and, thus, of its mechanical properties, such as hardness. For these reasons, a large variety of different materials can form superhard nanocomposites but only those systems which consist of refractory elements or compounds will show a sufficient hardness. This is very important criterion for the materials selection because for example nanocomposites, such as nc-M_nN/a-CN_x (Me = Ti, Zr) or M_nN/M' (M = Ti, Cr, Zr, M'= Cu, Ni.) can reach a hardness of 40 GPa but their thermal stability is expected to be limited to few 100 °C [24]. However Musil reports that the superhard Zr-Cu-N film exhibits thermal stability up to 900 °C. This means that the thermal stability of the structure of the Zr-Cu-N film is high. The experiment shows that the thermal stability of nanocomposites of the type nc-MeN/M´ can be high and comparable with that of nanocomposites composed of two hard phases, i.e. with that of the type nc-MeN/a-Si_3N_4 [18].

2.2.1.1. Hall-Petch Effect

Strengthening of polycrystalline materials by grain size refinement is technologically attractive because it generally does not adversely affect ductility and toughness. The classical effect of grain size on yield stress can be explained by a model invoking a pile-up of dislocations against grain boundaries, which results in dependence of the hardening increment on the square root of the grain size D:

$$\sigma_c = \sigma_0 + \frac{k}{\sqrt{D}} \tag{2.2}$$

where k is a constant. This is the classical Hall-Petch effect.

Whereas many metallic materials obey such a relationship over several orders of magnitude in grain size, it is inevitable that the reasoning behind equation (2.2) must break down for very small grains. A clear limit for the occurrence of dislocation plasticity in a polycrystal is given by the condition that at least one dislocation loop must fit into an average grain [Figures 2.2(a) and 2.2(b)]. The characteristic length, i.e. the loop diameter, must now be compared with the grain size D as the relevant size parameter:

$$d(\tau) = D \tag{2.3}$$

or

$$\tau = \frac{2T_d}{bD} \approx \frac{Gb}{D} \tag{2.4}$$

Figure 2.2(c) illustrates schematically this limit on Hall-Petch behavior: conventional grain size strengthening can be expected only to the right of the heavy line which signifies the limiting condition (2.3-2.4).

The plastic behavior of nanocrystalline materials with grain sizes below the critical value is not fully clear. Some authors also report an inverse Hall-Petch effect; others find insensitivity to grain size or a reduced Hall-Petch constant k in this range. It has been argued that because of the viscous behavior of amorphous materials (which can be considered the limiting case for grain refinement) the grain size strengthening effect will have to be reversed once the grain size D starts to approach the grain-boundary thickness, δ_b.

One possible explanation for such a softening effect comes from a reconsideration of the line tension T_d in equation (2.4). The more refined expression contains a lower (r_0) and an upper (r_1) cut-off distance for the stress field of the dislocation. In conventional materials r_1 generally lies in the micrometer range and therefore significantly exceeds r_0; this justifies replacing the logarithmic term by a constant. However, in nanocrystalline materials it is reasonable to equate r_1 to the grain size, which now gives $r_1 \approx r_0$ and makes T sensitive to the value of the grain size D. Therefore, we now have a case in which the characteristic length (d) is a function of the size parameter (D).

The resulting strength increment is given by

$$T_d = \frac{Gb^2}{4\pi} \ln \frac{r_1}{r_0} \tag{2.5}$$

This expression vanishes rapidly as the grain size D approaches the lower cut-off distance r_0. An even more refined expression has been obtained by Scattergood and Koch. They draw upon Li's model for the generation of dislocations from grain-boundary sources: as the dislocation density rescales inversely with grain size D, the obstacle spacing is

$$L \sim \frac{1}{\sqrt{\rho}} \sim \sqrt{D} \tag{2.6}$$

which yields

$$\tau = \frac{Gb}{2\pi D} \ln \frac{D}{r_0} \tag{2.7}$$

This expression, which is schematically shown as a dotted line in Figure 2.2(c), reduces correctly to Hall-Petch behavior for D [26].

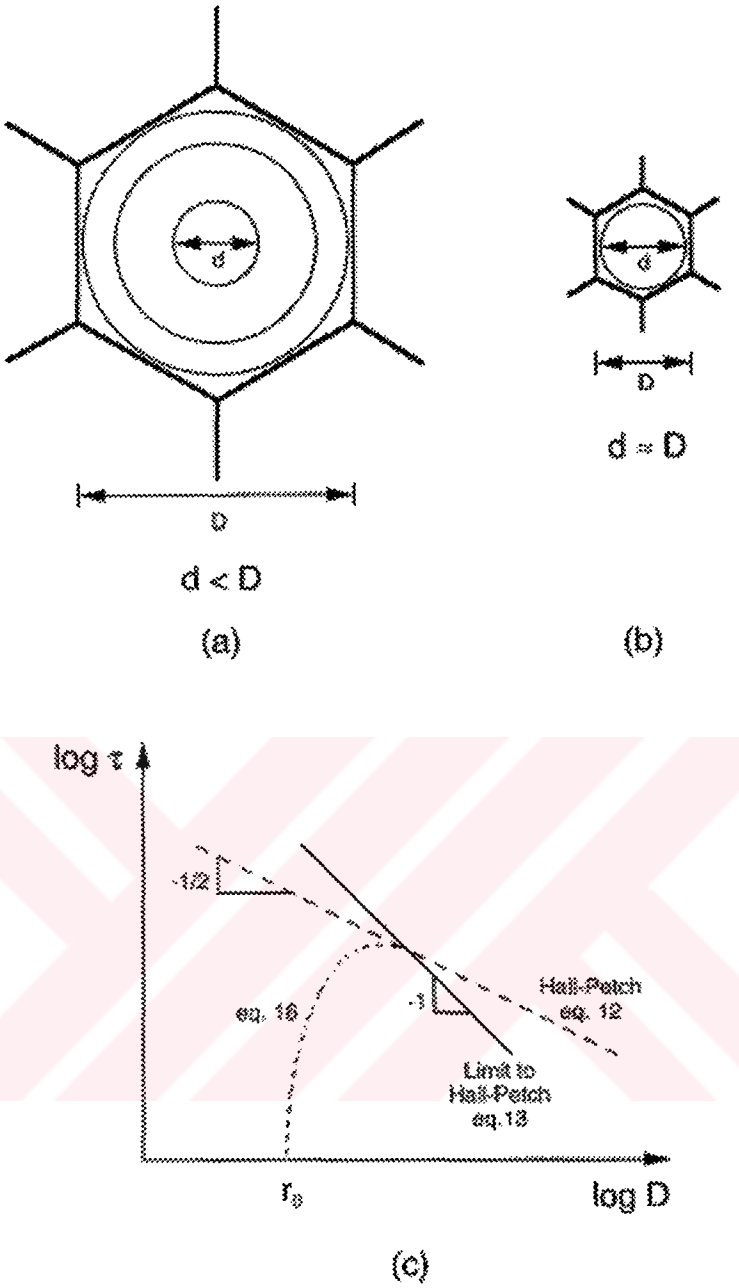

Figure 2.2 Grain size strengthening as explained by pile-ups of dislocation loops against grain boundaries (a). This mechanism must break down when the diameter d of the smallest loop no longer fits into a grain of size D (b). The limiting condition is shown as the heavy line in (c) where the shear strength t is plotted schematically as a function of grain size D. Hall-Petch behavior can only be found to the right of this line; abnormal or inverse behavior may result otherwise. The dotted line reflects schematically the Scattergood-Koch equation [equation (2.7)] [26].

2.2.1.2. Griffith Theory

Griffith theory of crack growth, which applies to brittle glasses and ceramics may yield a similar dependence of the critical fracture (crack growth) stress on the grain size as Hall-Petch relation. Accordingly, the critical stress σ_c for the growth of a

microcrack of a size a (a flaw usually originating from the sample preparation) is given by Eq. (2.8)

$$\sigma_c = k' \sqrt{\frac{2.E.\gamma_s}{k''.\pi.a_0}} \tag{2.8}$$

Here, E is the Young modulus, g the surface cohesive s energy, k9 and k0 are constants which depend on the nature of the microcrack and the geometry of the load. In well-compacted sample, the maximum size of the microcracks scales with the grain size. For these reasons the universality of the Hall–Petch strengthening is due to variety of different fracture mechanisms which all give more or less a similar increase of the strength and hardness with decreasing grain size. Different mechanisms can yield apparently the same dependence in different materials [27].

2.2.1.3. Koehler Theory

As suggested by Koehler, a strengthening effect can be obtained by using alternate layers of materials with high and low elastic modulus. Dislocations in soft material have lower deformation energy than dislocations in hard material. In a multilayered structure consisting of one hard and one soft alternating layer has deformation energy maximum in the hard layer and minimum in the soft one. If there is enough difference between elastic modulus of hard and soft layers, dislocations are trapped in soft layer and cannot pass to the hard one. Therefore strength and toughness of multilayered materials increases [28].

3. MAGNETRON SPUTTERING

Magnetron sputtering has developed rapidly over the last decade to the point where it has become established as the process of choice for the deposition of a wide range of industrially important coatings. The driving force behind this development has been the increasing demand for high-quality functional films in many diverse market sectors. In many cases, magnetron sputtered films now outperform films deposited by other physical vapor deposition (PVD) processes, and can offer the same functionality as much thicker films produced by other surface coating techniques. Consequently, magnetron sputtering now makes a significant impact in application areas including hard, wear-resistant coatings, low friction coatings, corrosion-resistant coatings, decorative coatings and coatings with specific optical or electrical properties.

The basic sputtering process has been known and, despite its limitations, used for many years. The introduction of conventional or balanced magnetrons in the early 1970s was an important step forward in overcoming these limitations. However, it was the development of the unbalanced magnetron in the late 1980s and its incorporation into multi-source closed-field systems in the early 1990s that transformed the capabilities of this technique, and has subsequently been responsible for its rise in importance. Closed-field unbalanced magnetron sputtering (CFUBMS) is an exceptionally versatile technique, suitable for the deposition of high-quality, well-adhered films of a wide range of materials at commercially useful rates.

The pulsed magnetron sputtering (PMS) process is another very important recent development in the sputtering field. The DC reactive sputtering of fully dense, defect-free coatings of insulating materials, particularly oxides, is highly problematic. The process is hampered by low deposition rates and the occurrence of arc events at the target, which are detrimental to the structure, properties and composition of the coating. However, pulsing the magnetron discharge in the mid-frequency range (10-200 kHz) has been found to prevent arc events and stabilize the

reactive sputtering process. High-quality oxide coatings can now be deposited using the PMS process at rates approaching those achieved for metallic coatings.

In all PVD processes, ion bombardment of the growing film is a critical parameter which strongly influences the structure and properties of the growing film. In a magnetron sputtering system, for any given set of deposition conditions, the ion current delivered to the growing film depends on the strength and design of the magnetic array in the magnetron. Clearly, in most cases this is fixed. However, new magnetrons have now been developed in which the magnetic array can be varied in situ without the use of electromagnets. This facility allows the ion current to the substrate to be controlled and optimized at all stages of the deposition process [29].

3.1. Types of Magnetron Sputtering

3.1.1. Conventional Magnetron Sputtering

In the basic sputtering process, a target (or cathode) plate is bombarded by energetic ions generated in glow discharge plasma, situated in front of the target. The bombardment process causes the removal, i.e., sputtering, of target atoms, which may then condense on a substrate as a thin film. Secondary electrons are also emitted from the target surface as a result of the ion bombardment, and these electrons play an important role in maintaining the plasma. The basic sputtering process has been known for many years and many materials have been successfully deposited using this technique. However, the process is limited by low deposition rates, low ionization efficiencies in the plasma, and high substrate heating effects. These limitations have been overcome by the development of magnetron sputtering and, more recently, unbalanced magnetron sputtering.

Magnetrons make use of the fact that a magnetic field configured parallel to the target surface can constrain secondary electron motion to the vicinity of the target. The magnets are arranged in such a way that one pole is positioned at the central axis of the target and the second pole is formed by a ring of magnets around the outer edge of the target. Trapping the electrons in this way substantially increases the probability of an ionizing electron-atom collision occurring. The increased ionization efficiency of a magnetron results in a dense plasma in the target region. This, in turn, leads to increased ion bombardment of the target, giving higher sputtering rates and,

therefore, higher deposition rates at the substrate. In addition, the increased ionization efficiency achieved in the magnetron mode allows the discharge to be maintained at lower operating pressures and lower operating voltages than is possible in the basic sputtering mode.

The differences in design between a conventional magnetron and an unbalanced magnetron are only slight. However, the difference in performance between the two types of magnetron is very significant. In a conventional magnetron the plasma is strongly confined to the target region. A region of dense plasma typically extends some 60 mm from the target surface. Films grown on substrates positioned within this region will be subjected to concurrent ion bombardment, which, as mentioned earlier, can strongly influence the structure and properties of the growing film. Substrates placed outside this region, however, will lie in an area of low plasma density.

Consequently, the ion current drawn at the substrate (typically, <1 mA/cm^2) is generally insufficient to modify the structure of the film. The energy of the bombarding ions can be increased by increasing the negative bias applied to the substrate. However, this can lead to defects in the film and increased film stress, and therefore, be detrimental to the overall film properties. Thus, it is difficult to deposit fully dense films on large or complex components using conventional magnetrons.

To deposit dense films without introducing excessive intrinsic stresses, a high flux (>2 mA/cm^2) of relatively low energy (<100 eV) ions is generally preferred. These conditions are readily provided by unbalanced magnetrons [29].

3.1.2. Unbalanced Magnetron Sputtering

In an unbalanced magnetron the outer ring of magnets is strengthened relative to the central pole. In this case, not all the field lines are closed between the central and outer poles in the magnetron, but some are directed towards the substrate, and some secondary electrons are able to follow these field lines. Consequently, the plasma is no longer strongly confined to the target region, but is also allowed to flow out towards the substrate. Thus, high ion currents can be extracted from the plasma without the need to externally bias the substrate. Earlier studies had shown that in some magnetron designs not all the field lines closed in on themselves (indeed, very few, if any, magnetrons are truly fully balanced). However, it was Windows and

Savvides who first appreciated the significance of this effect when they systematically varied the magnetic configuration of an otherwise conventional magnetron. They, and other researchers, have subsequently shown that substrate ion current densities of 5 mA/cm^2 and greater, i.e., approximately an order of magnitude higher than for a conventional magnetron, can be routinely generated when using an unbalanced magnetron. A comparison between the plasma confinements obtained in different magnetron modes is shown schematically in Figure 3.1.

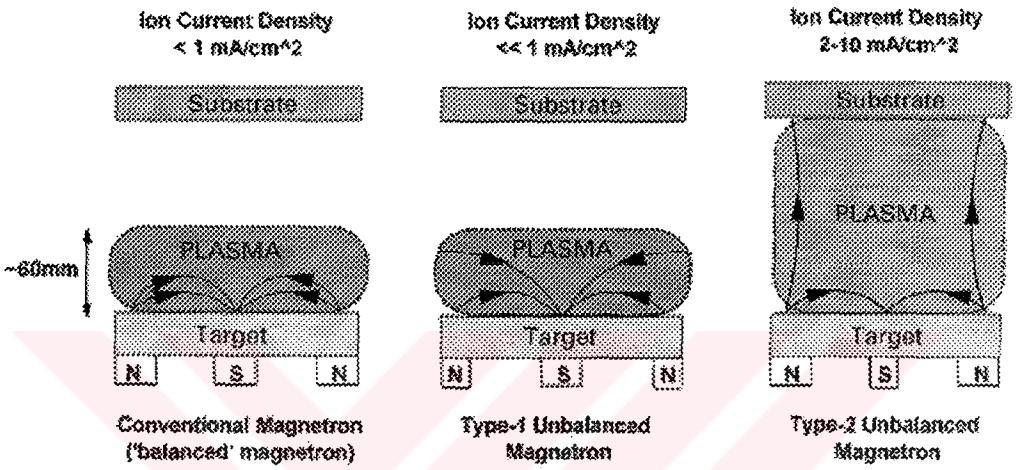

Figure 3.1 Schematic representation of the plasma confinement observed in conventional and unbalanced magnetrons. [29]

Thus, in addition to providing a high flux of coating atoms (compared to a basic sputtering source), an unbalanced magnetron also acts as a very effective ion source. Furthermore, the ion current drawn at the substrate is directly proportional to the target current. Deposition rate is also directly proportional to target current. As a result, and unlike other ion-plating processes, the ion-to-atom arrival ratio at the substrate remains constant with increasing deposition rate.

The design of unbalanced magnetron discussed above was termed type-2 by Window and Savvides. However, they also considered the opposite case (type-1), where the central pole was strengthened relative to the outer pole. In this case the field lines which do not close in on themselves are directed towards the chamber walls and the plasma density in the substrate region is low (see Figure 3.1). This design is not commonly used, because of the resulting low ion currents at the substrate [29].

3.1.3. Closed-Field Unbalanced Magnetron Sputtering

Despite the benefits offered by unbalanced magnetrons, it is still difficult to uniformly coat complex components at acceptable rates from a single source. Therefore, in order to commercially exploit this technology, multiple magnetron systems have been introduced.

In a multiple magnetron system, the magnetic arrays in adjacent magnetrons can be configured with either identical, or opposite magnetic polarities. In the former case the configuration is described as mirrored and in the latter case closed field, and both configurations are shown in Figure 3.2. In the mirrored case, the field lines are directed towards the chamber walls. Secondary electrons following these lines are lost, resulting in a low plasma density in the substrate region. Conversely, in the closed field configuration, the field lines are linked between the magnetrons. Losses to the chamber walls are low and the substrate lies in a high density plasma region [29].

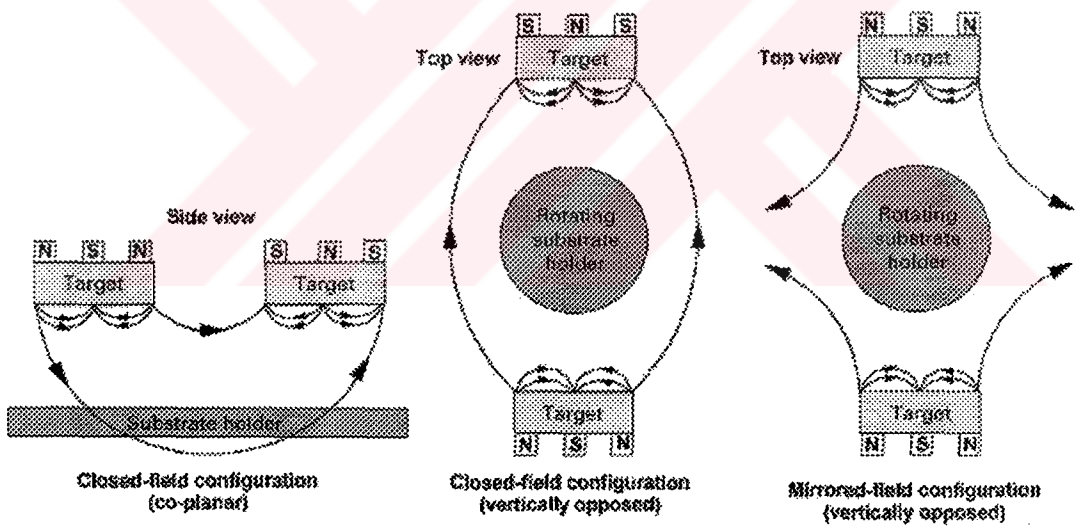

Figure 3.2 Dual unbalanced magnetron configurations. [29]

3.1.4. Pulsed Magnetron Sputtering

The pulsed magnetron sputtering (PMS) process has transformed the production of highly insulating films, particularly oxides such as alumina. Oxide coatings can be produced by the reactive magnetron sputtering of a metallic target in a controlled oxygen atmosphere. They can also be produced by the direct RF (radio frequency; usually 13.56 MHz) sputtering of an oxide target. However, both of these processes are problematic. RF sputtering can produce high-quality films, but deposition rates

are very low (typically in the μm/h range). Also, RF sputtering systems are complex and difficult to scale up for commercial applications.

The problems associated with the reactive magnetron sputtering of highly insulating materials are widely reported. As the deposition process proceeds, areas on the target away from the main racetrack become covered with an insulating layer, as do the target earth shields. This coverage of the target with the reaction product is referred to as target poisoning. The poisoned layers charges up, until breakdown occurs in the form of an arc. Arc events at the target can result in the ejection of droplets of material from the target surface. The ejected material can cause defects in the growing film, which are particularly detrimental to the performance of optical or corrosion-resistant films. Also, the damaged area on the target may become a source of further arc discharges, leading to an increasing frequency of arcing. The reactive sputtering process is controlled by a feedback loop. Arc events prevent stable operation of the process by causing rapid fluctuations in the deposition parameters. This, in turn, can affect the stoichiometry of the growing film. In summary therefore, arc events during reactive sputtering are a serious problem, because they can affect the structure, composition and properties of the growing film, and can also lead to damage of the magnetron power supply.

The recently developed pulsed magnetron sputtering process (PMS) overcomes many of the problems encountered when operating in the reactive sputtering mode. It has been found that pulsing the magnetron discharge in the medium frequency range (10-200 kHz) when depositing insulating films can significantly reduce the formation of arcs and, consequently reduce the number of defects in the resulting film. Furthermore, deposition rates during pulsed reactive sputtering approach those obtained for the deposition of pure metal films, i.e., of the order of tens of microns per hour. The PMS process, therefore, now enables the high rate deposition of defect-free ceramic films. As such, this process has attracted considerable commercial interest, and has led to the development of a new generation of magnetron power supplies and pulse units.

Although AC power supplies are becoming available, the PMS process generally utilizes pulsed DC power. In this case, the target is sputtered at the normal operating voltage (typically, -400 to -500 V) for a fixed pulse-on time. The pulse-on time is limited, such that charging of the poisoned regions does not reach the point where

breakdown and arcing occurs. The charge is then dissipated through the plasma during the pulse-off period by switching the target voltage to a more positive value. There are two modes of operation: unipolar pulsed sputtering, where the target voltage is pulsed between the normal operating voltage and ground; and bipolar pulsed sputtering, where the target voltage is actually reversed and becomes positive during the pulse-off period. Due to the much higher mobility of electrons in the plasma than ions, it is usually only necessary to reverse the target voltage to between 10 and 20% of the negative operating voltage to fully dissipate the charged regions and prevent arcing (if the target voltage is not fully reversed, this mode should most accurately be described as asymmetric bipolar pulsed DC).

The PMS process has also been extended to dual magnetron systems. In this case, both magnetrons are attached to the same pulse unit, and the process is described as dual bipolar pulsed sputtering. Each magnetron acts alternately as an anode and a cathode. By operating in this manner, the anode and cathode surfaces are prevented from poisoning, and very long-term process stability is achieved (>300 h). Industrial applications of this process include the deposition of high-quality optical coatings on materials such as architectural or automotive glass and polymer web.

One final recent development in this field is the use of pulsed DC power at the substrate. Pulsing the substrate bias voltage has been found to significantly increase the ion current drawn at the substrate. In magnetron systems, the current drawn at the substrate normally saturates at bias voltages of the order of -100 V. Further increases in bias voltage do not lead to a further increase in current. It is generally assumed that the saturation current is an ion current, as any electrons approaching the substrate will be repelled at this voltage. Recent studies has shown that if the bias voltage is pulsed, not only is the magnitude of the saturation current greater than for the DC bias case, but the current drawn at the substrate continues to increase as the bias voltage is increased. The exact mechanism causing these effects is not yet clear. However, it is known that plasmas generated by oscillating fields are more energetic (i.e., have higher plasma densities and electron temperatures) than DC plasmas. Pulsing the substrate bias voltage, therefore, offers a novel means of controlling the ion current density drawn at the substrate. This could be utilized, both during deposition to optimize the coating structure and adhesion, and also during sputter

cleaning and substrate heating, where enhanced ion currents could allow shorter process times [29].

3.2. Control of Microstructure in Magnetron Sputtering

The film microstructure, phase and chemical composition can be controlled by two fundamental processes [30]:

1. Particle bombardment of the growing film.
2. Mixing effect, i.e. the incorporation of additional elements into a base material.

3.2.1. Ion Bombardment of Growing Film

The type of particles that can bombard the growing film varies with the gas pressure. The energy E_r, can be controlled either by the substrate bias U, in the case of ion bombardment or by the gas pressure p in the case of fast neutrals bombardment, or by a combined action of both U, and p. The particle bombardment can be classified as follows:

1. Inert gas ions (p>0.1 Pa)
2. Combined action of inert gas and fast neutrals at (10^{-2}<10^{-1} Pa)
3. Ions of sputtered material

The energy of ions E, bombarding the growing film or surface to be modified can vary in a very wide range from eV to MeV. According to the magnitude of E; we can distinguish two basic processes:

1. Magnetron sputter ion plating (MSIP) process which is based on low-energy ion bombardment (E_i ranges from several eV to about 1000 eV) of the growing film.
2. Ion implantation or plasma immersed ion implantation which uses a high-energy ion bombardment (E_i>>keV) for the modification of the surface layer of material or the growing film, respectively.

The low-energy particle bombardment is widely used in sputter deposition of thin films. The principle of film modification by low-energy particle bombardment is shown in Figure 3.3. The particles that may occur in the MSIP process are: (i) Ar^+

reflected from the target, (ii) Ar^+ and M^+ ions accelerated from the plasma, (iii) energetic Ar and M (atoms of sputtered metal target) neutrals created in consequence of charge exchange and (iv) negative ions emitted from the surface of oxide targets.

The effect of ion bombardment is determined by the energy per deposited atom E_p defined, in the simplest case of the ion plating process and non-reactive deposition, as

$$E_p = \frac{E_i \nu_i}{\nu_m} = \frac{e(U_p - U_s)\nu_i}{\nu_m} \tag{3.1}$$

where E; is the energy of ions, ν_i and ν_m are fluxes of ions bombarding the growing film and coating particles, respectively, U_p is the plasma potential, U_s, is the substrate bias, i_s, is the substrate ion current density, a_D is the deposition rate and e is the elementary charge.

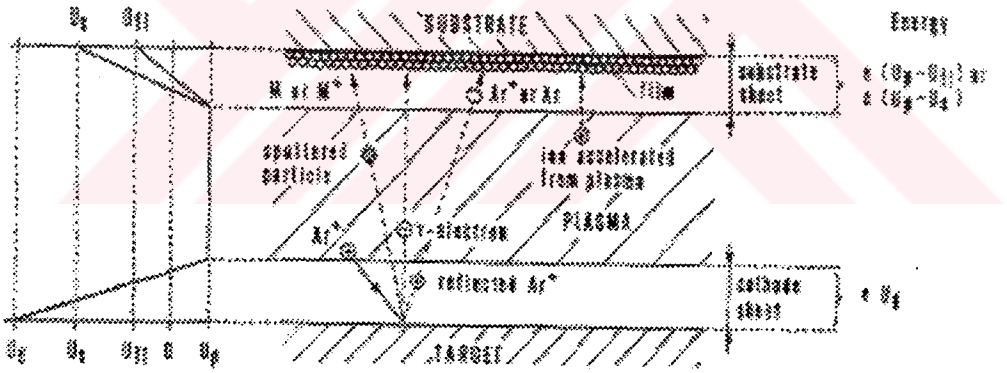

Figure 3.3. Schematic diagram of basic particles and potentials in the low-pressure discharge used for MSIP of thin film. U_d, U_{fl} and U_p is the discharge voltage, the floating potential and plasma potential, respectively. [30]

Every material can be characterized by a certain critical value $E_p=E_c$. The films produced at $E_p<E_c$ are porous, soft, have a matt appearance and are in tension. On the contrary, films produced at $E_p>E_c$ are compact, dense, have a smooth surface, exhibit high reflection and are in compression. The films produced at $E_p=E_c$ exhibit zero stress. The same value of E_p, however, does not correspond to the same microstructure of the film. Therefore, it is necessary to note that the parameters E_i and ν_i/ν_m are not physically equivalent [30].

3.2.2. Mixing Effect

The so called mixing effect, i.e. the addition of one or several elements into a base one element film, plays an important role in the magnetron sputtering of thin films. The mixing effect opens new possibilities in sputtering. The amount and type of the additional elements (AE) can be used

1. To control the orientation (texture) and size of grains in the sputtered film.
2. To form nanocrystalline and amorphous film.
3. To form high-temperature (HT) structures at low temperatures T of about or below 100 °C.

The main parameters which can be used to control the film structure are the amount and type of added elements. A substantial role in the formation of nanocrystalline films is played by the following factors.

1. The mutual miscibility or immiscibility of the film elements.
2. The ability of the elements to form solid solutions or intermetallic compounds.
3. The enthalpy of alloy formation ΔH, (negative or positive).

Which structure of the alloy films will arise strongly depends on these factors and their mutual combination.

The mixing process is an efficient method convenient for production of nanocrystalline and amorphous alloy films. Comparing with ion bombardment, no substrate bias and heating are necessary to form the films with nanocrystalline structures and metastable crystalline high-T phases can be sputtered on unheated substrates. This is connected with the atomic scale heating of the growing film by the sputtered particles (the kinetic energy of about 10 eV) and subsequent extremely rapid cooling at an atomic level [31].

3.3. Structure Zone Models

Structure zone models clearly demonstrate that the structure is changing according to the deposition conditions and behaves systematically in a certain temperature range. The extensions of these models have been also carried out according to differences in various deposition techniques. The effect of sputtering

gas pressure has been considered in the model of Thornton and that of the bias voltage in the model of Messier. The backbone of these models is that they are constructed simply by the compilation of the results of the authors and only two elementary atomic processes, the surface diffusion and volume diffusion as well as their temperature dependencies were considered at the interpretation of the various structure zones. The zone boundaries are related to the set on of surface diffusion at about 0.1-0.2 T_m, which is the boundary between Zone I and T, and to the set on of volume diffusion at about 0.3-0.4T_m, which is the boundary between Zone T and II. Although the general behavior of the films can be described by these models, deviations in case of different materials and deposition conditions can be observed.

Experiments of the past and more recently the development and application of two component polycrystalline and nanocrystalline advanced materials made it clear that the incorporated impurities and intentionally introduced additives play a crucial role in the structure evolution of polycrystalline films and coatings, and can have drastic influence on the structure zones. In order to understand these phenomena one has to clarify by which mechanism do the impurities influence the structure evolution, and which are the characteristic structural features that appear as a result of impurity incorporation. For this reason one has to build the structure zone model by analyzing the role of the fundamental structure forming phenomena in the different structure zones. This analysis leads to two types of structure zone models describing the structure evolution characteristics of pure films with respect only to the substrate temperature (ideal structure zone model) and describing the effect of impurities and substrate temperature simultaneously (real structure zone model) (Figure 3.4) [32].

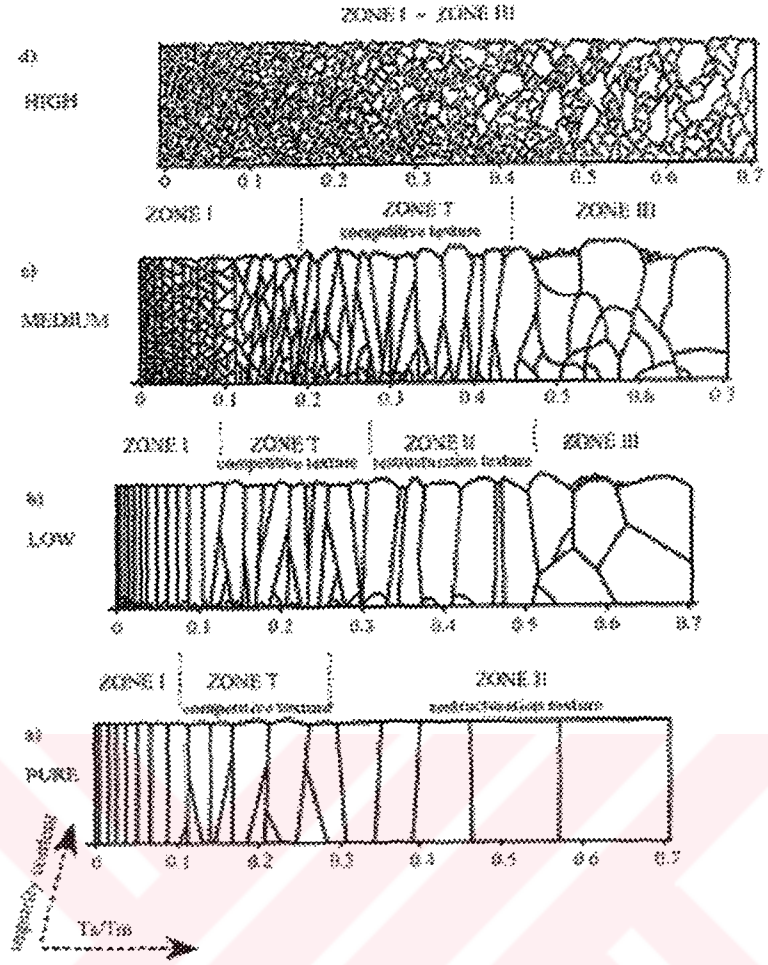

Figure 3.4 Ideal (a), and real structure zone models of low (b), medium (c), and high (d) impurity concentrations [32]

3.3.1. Zone I

At low substrate temperatures, below 0.1 T_m due to the high overcooling the nucleation density is extremely high. Because the impinging adatoms have no or extremely low surface mobility on the substrate surface they stick in the near vicinity where they fall. Neither coalescence nor grain boundary migration can occur, therefore the development of large grains is inhibited and the structure preserves the morphology inherited from the nucleation stage. The lateral grain size due to the nucleation density, and the texture if exists, is related to substrate effects. In the ideal case of pure material, the growth can proceed in vertical direction uninterruptedly; therefore fiber like porous structure develops. The growth structure is mainly determined by the fundamental structure forming phenomenon: nucleation.

In contaminated films the growth of grains follows the phenomena described by the ballistic models and fiber like structure develops. No segregation of the impurity species can take place and they will be incorporated into the growing fibers practically at their impinging sites [32].

3.3.2. Zone T

At substrate temperatures where the surface diffusion sets in, the fundamental structure forming phenomenon, which becomes decisive in determining the growth structure is the crystal growth. The film formation starts by the development of a small grained structure reflecting the nucleation density, due to immobile grain boundaries. When the film becomes continuous the surface diffusion makes possible the migration of adatoms between neighbouring grains, therefore the crystals having lower surface energy incorporate more material and grow over the neighbouring crystals having higher surface energy. This competitive growth results in the typical cone shaped columnar structure characteristic of this zone. The competitive growth has also influence on the texture of the films by selecting the faster growing directions as texture components. The upper zone boundary is determined by the onset of grain boundary migration.

In contaminated films the lower zone boundary shifts to higher temperatures as described in 3.3.1 Impurity incorporation can limit the grain boundary migration therefore the upper zone boundary is also shifted to higher temperatures. Impurities can have a peculiar effect on the texture evolution in case of competitive growth. If there is anisotropy in the surface chemical interaction of impurity species with the various crystal faces, at low or medium contamination level the growth of certain crystal faces can be blocked while others can grow, and this leads to the development of special preferred orientations.

In highly contaminated films the covering impurity phase can block the growth of all the crystals, consequently the competition can not evolve, Zone T does not appear and globular structure with grain boundaries covered and stabilized by the impurity phase will develop [32].

3.3.3. Zone II

At substrate temperatures where grain boundary migration sets in, columnar structure develops with columns proceeding from the substrate to the free surface of the film. The grain boundaries are generally perpendicular to the substrate surface. For this structure the responsible fundamental structure forming phenomenon is the grain growth. Due to grain boundary migration the initially formed small grained structure, characteristic of the nucleation density, is dissolved step by step during coalescence and in the later growth stages. The driving force of grain boundary migration is the grain boundary energy and the surface energy difference of the neighboring crystal faces due to their orientational relationships. Accordingly the texture evolution is related to the grain growth and the texture axis is related to the lowest surface energy. In the ideal case of pure films this zone represents the upper zone of the structure zone model. As the substrate temperature is increased the lateral size of grains is increased.

In contaminated films the grain boundary mobility is limited; therefore the lower zone boundary is shifted to higher temperatures as discussed in 3.3.2. At high temperatures (above 0.5Tm), Zone III appears presenting upper boundary for Zone II. Due to the limited grain boundary mobility the abnormal grain growth can not be completed, therefore bimodal grain size distribution will characterize the film. At increased contamination level the grain boundaries become immobile and Zone II disappears from the structure zone model [32].

3.3.4. Zone III

This zone appears only in contaminated films, and the grain size can extend from the globular (nanocrystalline) to the equiaxed micrometer sized range. The responsible fundamental structure forming phenomenon is the process induced segregation of impurities. By increasing the substrate temperature the grain size increases, therefore the surface to volume ratio decreases in the film. In this case the impurity species are segregated on a smaller surface area resulting in a faster development of a surface covering layer of impurities on the crystal surfaces. Due to this, the growth of the crystals is stopped and the growth continues by repeated nucleation. This leads to the typical equiaxed structure at high substrate

temperatures in case of low and medium level of impurity concentration. Since the grain growth is also limited in spite of the high temperature no or only week texture evolution can take place. By increasing the contamination level the lower boundary of Zone III is shifted to lower temperatures while at first Zone II and later Zone T will disappear gradually until the lower boundary of Zone III reaches the upper boundary of Zone I. In this case the part of Zone III at lower temperatures will exhibit the nanocrystalline structure [32].

4. MOLYBDENUM NITRIDE AND SILVER

4.1. Molybdenum Nitride

4.1.1. Interstitial Nitrides

The nitrides of the fourth to sixth group transition metals are distinguished from the others by their exceptional mechanical and electrical properties. In these compounds nitrogen atoms occupy interstitial lattice sites because they are much smaller than the refractory metal atoms. For this reason transition metal nitrides are often referred to as interstitial nitrides [33].

The interstitial nitrides provide an ample range of properties that can be tailored to optimize the desired functionality. They are hard and having good wear-resistance and chemical resistance. They are important industrial materials and have a significant number of major applications in cutting and grinding tools, wear surfaces, semiconductors, and others. The interesting physical properties of thin films of transition metal compounds have made them extremely useful for such applications as wear and corrosion resistant coatings and diffusion barriers in semiconductor metallization [34].

Interstitial nitrides are crystalline compounds of a host metal and nitrogen where the nitrogen atom occupies specific interstitial sites in the metal structure which are generally close packed. This configuration places a low limit on the size of the metal atom in order for the nitrogen atom to fit in the available sites of the metal structure. The metals of the nine early-transition elements, i.e. titanium, zirconium, and hafnium of group IV, vanadium, niobium, and tantalum of Group V, and chromium, molybdenum and tungsten of Group VI, fit the criteria of size and site availability, and form interstitial nitrides [35].

The interstitial nitrides rarely exhibit ideal stoichiometry. Each binary phase has an extended composition range with varying metal to nonmetal ratio and significant vacancy concentration. Generally, appreciable vacancy concentrations are found on the nonmetal lattice sites and to a lesser extent on the metal lattice sites. The

presence of large concentration of vacancies has a profound effect on the properties of the nitrides. The thermodynamic, mechanical, electrical, magnetic, and superconducting properties of these phases are all dependent on their defect structure. The interstitial nitrides also can tolerate metal atom vacancies. This means that, if the metal-atom vacancies are more numerous than the nitrogen-atom vacancies, the nitrogen-to-metal ratio will be greater than 1. As a result, the structure of interstitial nitrides is somewhat difficult to identify with certainty.

Interstitial nitrides have a complex electronic bonding system, which includes metallic, covalent, and ionic components. Similar to ceramic, they have high hardness and strength. Like metals, they have high thermal and electrical conductivity. Interstitial nitrides are susceptible to the presence of even minute amounts of impurities, particularly oxygen, which tend to distort the structure

There are two types of interstitial sites in the close-packed structure of early transition metals, i.e., the tetrahedral sites and the octahedral sites. The nitrogen atoms occupy only the octahedral sites since the tetrahedral sites are too small to accommodate them. There is one octahedral site per atom of the host metal. In 1931, Hagg formulated an interesting set of empirical rules regulating the crystal structure types formed by transition-metal carbides, nitrides, borides, and hydrides. Although minor exceptions to the rules have been found, their general features remain valid. According to Hagg, the structure of transition-metal carbides, nitrides, borides, and hydrides is determined by the radius ratio $r=r_x/r_{Me}$. Here the r_x and r_{Me} are the radius of the interstitial and transition metal atom, respectively. If r is greater than 0.59, the transition metal and interstitial elements form complicated structures. If r is less than 0.59, the metal atoms form very simple structures: A1, A2, A3, or simple hexagonal. When r is less than 0.59, the light elements are accommodated in the largest interstitial sites of the relatively simple metal host structure. The interstitial site must be smaller than the interstitial atom that it accommodates, otherwise there will be insufficient bonding between the metal and nonmetal atoms and the structure will become unstable. On the other hand, the interstitial site cannot be too much smaller than the interstitial atom, otherwise the presence of the metal-metal interactions will expand the metal host lattice to the point where the metal-metal interaction will become weak and the structure will lose its stability. Table 4.1 lists the nitrogen/metal atomic radii ratio of interstitial nitrides [34]. As shown in the table,

molybdenum nitride is qualified as the host structure for interstitial nitrides, since the ratio of the radius of the nitrogen atom to that of the atom of the host metal is 0.534, which is less than 0.59.

Table 4.1 Nitrogen/Metal atomic radii ratio of interstitial nitrides [35]

Group IV	Group V	Group VI
Ti-N 0.504	V-N 0.553	Cr-N 0.584
Zr-N 0.463	Nb-N 0.508	Mo-N 0.534
Hf-N 0.467	Ta-N 0.508	W-N 0.531

4.1.2. Molybdenum Nitride

Figure 4.1 is the phase diagram of the Mo-N system. Molybdenum forms a variety of nitrogen-containing compounds MoN_x with X ranging from 0 to 1. The JCPDS powder diffraction files [36] report five phases for bulk Mo-N compounds. These include the hexagonal δ-Mo_2N, fcc γ-Mo_2N, two body center tetragonal Mo_2N phases (β1 and β2) and tetragonal $Mo_{16}N_7$. As shown in Figure 4.2, face-centered cubic γ-Mo_2N has a lattice parameter of 0.1463 nm. The crystal structure is NaCl type where the Mo atoms occupy the positions of the fcc lattice points and nitrogen atoms occupy 50% of the total octahedral sites [37]. The B1-Mo-N film which is not an equilibrium phase but has good super-conductivity properties also has been reported literatures [38]

Like most of the other early transition metals, pure Mo has a bcc structure which cannot geometrically accommodate nitrogen atoms in its interstices. To form a nitride, the metal must switch to a close-packed structure (fcc or hcp) so that the larger octahedral sites can accommodate nitrogen atoms. The switch is accompanied by an increase of a few percent in the distance between the metal atoms.

γ-Mo_2N is an interstitial transition metal nitride with a Hagg's structure. In Hagg's structures, when the N/Me ratio is less than 0.59, metal atoms form simple structural interstitial compounds and nitrogen atoms are accommodated in the largest interstitial sites of the simple structure. On the other hand, the interstitial site cannot be too much smaller than the interstitial atom; otherwise the presence of the

interstitial atom will expand the metal host lattice to the point where the metal-metal interaction will become weak and the structure will lose its stability. For γ-Mo_2N the Mo atom formed the fcc lattice structure and nitrogen takes up half of the octahedral sites with the N/Mo atomic radius ratio of 0.534. Table 4.2 shows the radius ratio of metal atoms to nitrogen atoms of different interstitial nitride groups. For IV group transition metal nitride e.g. Ti-N, the N/Me atomic radius ratio is much smaller compared with that of the VI group transition metal nitrides e. g. Mo-N, so the octahedral interstitial sites formed by group VI transition metals (e.g. Mo) atoms is much smaller than that of group IV transition metals (e.g. Ti). Interstitial compounds tend to be non-stoichiometric in nature; the population of the occupied octahedral sites determines the stoichiometry of the compound. As for TiN, under high nitrogen partial pressure, the stoichiometric atomic ratio of N/Ti for TiN_x can go beyond 1.0 without damaging the fcc structure, but for the MoN_x, as the octahedral site formed by Mo is much smaller than that of Ti, as more nitrogen incorporated into the lattice site, the excess nitrogen atoms will expand the Mo host lattice further, thus the Mo-Mo interaction becomes weak and the structure loses stability and evolves into amorphous structure [34].

Table 4.2 The atomic radius ratio of nitrogen atom to metal atoms [34]

	IV Group			**V Group**			**VIGroup**		
Elements	Ti	Zr	Hf	V	Nb	Ta	Cr	Mo	W
Atomic radius (Å)	1.467	1.597	1.585	1.338	1.456	1.457	1.267	1.386	1.394
N/Me radius ratio	0.504	0.463	0.467	0.553	0.508	0.508	0.584	0.534	0.531

4.1.3. Applications of Molybdenum Nitride

Like the other transition metal interstitial nitrides, molybdenum nitride has many exceptional mechanical and exceptional electrical properties such as high wear and corrosion resistance, high electrical and thermal conductivity and high chemical stability. Besides the chemical and physical properties that are similar to the other

interstitial nitrides, molybdenum nitride has its unique electronic, magnetic and catalytic properties. γ-Mo_2N is the most predominate crystalline phase in most Mo nitride powder catalysis because the Mo atoms in γ-Mo_2N are arranged in an fcc cubic array with nitrogen atoms randomly distributed in half of the octahedral interstices. This results in a Mo-Mo bond expansion from 272 to 417 pm to induce a d-band contraction and an increase of the density of state at the Fermi level of the molybdenum atoms, leading to the resemblance of the nitride to the group VIII metals in electronic, magnetic and catalytic properties [39]. Molybdenum nitride is a prospective candidate for high-T superconductor and diffusion barrier of microelectronic industry.

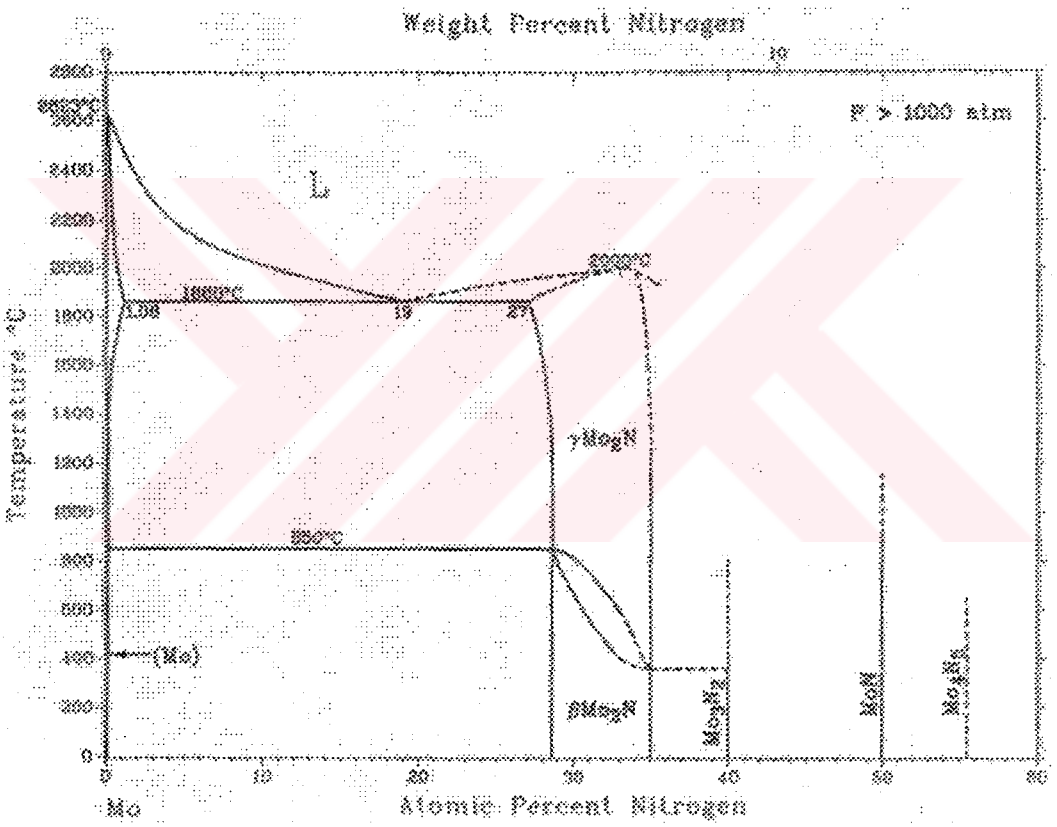

Figure 4.1 Phase diagram of Mo-N system [36].

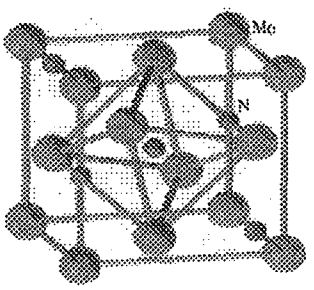

Figure 4.2 Crystal structure of γ-Mo_2N [38].

4.1.4. Preparation Methods

The bulk molybdenum nitride material is widely used in catalysis industry for a number of hydrogenation reactions such as ammonia synthesis, hydrogenolysis, etc. The most common preparation techniques for high surface area γ-Mo_2N catalysis are nitridation of massive Mo (foil, powder) by molecule nitrogen or NH_3 or reduction of MoO_3 with NH_3 or H_2 and N_2 mixture in a temperature programmed manner [40]. Molybdenum nitride thin films have been prepared by both PVD and CVD methods. CVD method generally involves a high temperature process and crystalline structures are often observed. The presence of impurities is also a problem with CVD methods. For PVD methods, non-equilibrium processes are often involved and result in both amorphous and nanocrystalline structure formation. The deposition rate of the CVD method is much higher than that of the PVD methods, thus thicker films are often obtained by CVD methods, whereas thin and high purity films can be prepared by PVD methods.

The PVD method for preparation of molybdenum nitride include: a) Reactive sputter deposition [37, 40-42]; b) Ion beam assisted deposition [43]; c) Cathodic arc plasma deposition [1]; d) Laser-promoted nitridation [33]; and e) Electron beam evaporation [44].

The CVD method also has been employed to prepare molybdenum nitride thin films have by different routes: Renaud Fix et al [33] report low temperature atmospheric pressure metal-organic chemical vapor deposition of amorphous molybdenum nitride thin films by reaction of $Mo(N(CH_3)_2)_4$ with NH_3. S.L Roberson et al [45] deposited the molybdenum nitride thin film by reaction of the $MoCl_6$ or $Mo(CO)_6$ with NH_3. M. Maoujoud et al. [46] obtained molybdenum nitride thin films by reacting evaporated Mo with nitrogen at 1023 K.

4.2. Silver

Nowadays, mechanical materials are commonly requested to possess various properties such as good tribological properties, high hardness and corrosion resistance according to development of industrial fields. The solid lubrication has an important role in the fields of tribology such as space-age transportation system, semiconductor industry in vacuum condition, advanced heat engine, and atomic

energy requiring high and extremely low temperature [47]. Solid lubricants commonly used are MoS_2, WS_2, Pb and Ag [48].

Generally, silver is known to have low shear strength, a good transfer forming tendency, corrosion resistance, and high electrical and thermal conductivity. Furthermore, silver films produce fewer wear particles and outgas than any other material for solid lubricant while being used in a vacuum condition [47].

The use of the noble metal silver is appealing, since it is known to form coatings with good friction characteristics and in fact, a substantial increase in the wear resistance and a significant decrease in friction coefficient have been observed in carbon films with encapsulated silver clusters of nanometer size [10].

In literature it was shown that silver can form nanocomposite composite with nitrides and carbides such as TiN, TiC and WC and improves the hardness and tribological properties of these coatings [9, 10].

In the study of Acros et al. Ag can easily form a nanocomposite coating with TiN [10]. Endrino et al. reported that incorporation of Ag into TiC films decreases the friction coefficient down to 0.2 as the Ag content increased up to 15 at %. Further increment of Ag content increased the friction coefficient [48]. In another study of Endrino et al. it was shown that the friction coefficient of WC coatings decreased down to 0.2-0.4 with increasing silver content up to 39 at % and in TiC coatings friction coefficient was decreased down to 0.26 with the silver content increased up to 51 at %. Further increase of silver content increased the friction coefficients of both WC and TiC coatings [10]. Gulbinski et al. reported that Ag doped MoO_3 coatings have the friction coefficients between 0.35 and 0.2 while MoO_3 coating has the friction coefficient of 0.45. In the same study Ag dopped V_2O_5 coatings show satisfactory results [12]. In the study of Endrino et al. it is cited that Cheng et al. examined thin films of a hard metal (Mo, Ni) combined with Ag, as well as metal nitride/Ag, and found they exhibited good wear properties along with lower friction when tested in air environments [48].

Ag_2O thermally decomposes to Ag and O_2 temperatures about 412 K (182 °C) according to equation (4.1) [49]. This property can be used to improve tribological properties at high temperatures.

$$2Ag_2O \xrightarrow{400K(182°C)} 4Ag + O_2 \qquad \text{(Eq. 4.1)}$$

4.3. Molybdenum-Silver System

Molybdenum and silver are immiscible metals. Phase diagram of molybdenum silver system is given in Figure 4.3 [36]. Molybdenum is insoluble in solid silver, but in the liquid state, silver can dissolve 5.6 at % Mo at about 1600 °C. Several percent of molybdenum are soluble in silver at 1400 °C. Molybdenum is not soluble in silver. The maximum solid solubilities at 958.5 °C are 0.15 at % molybdenum in silver and 0.00578 at % silver in molybdenum.

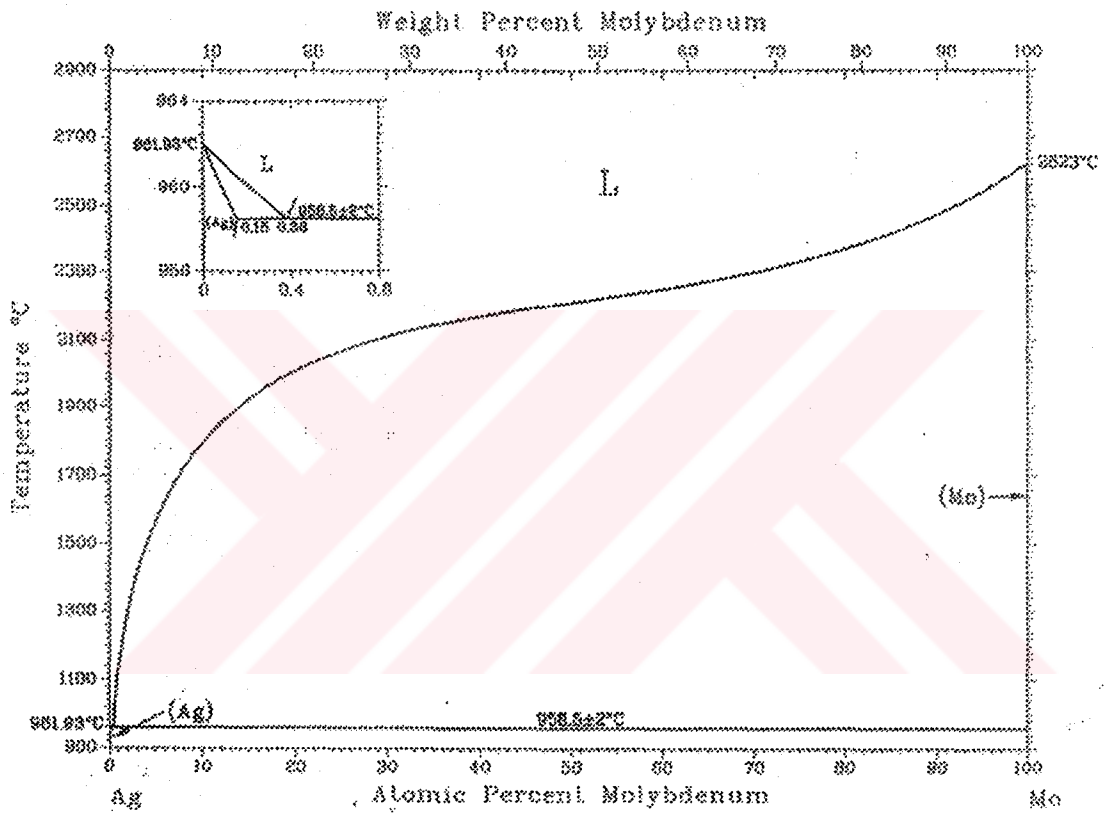

Figure 4.3 Phase diagram of Ag-Mo system [36].

5. FRICTION AND WEAR

5.1. Definitions

Friction and wear are elements of the field of tribology. Tribology is a discipline involving the physics, chemistry and engineering of moving and contacting bodies. Friction is defined as the resistance to relative motion between two surfaces in contact and wear is the volume loss and/or damage resulting from that contact [50]. Friction and wear are not intrinsic materials properties but are characteristic of a tribosystem. Friction and wear of sliding pairs can be divided into 5 categories:

i. Micro-geometrical pairing properties.

ii. Loading and macro-geometrical properties

iii. Tribomechanical properties

iv. Environmental properties

v. Metallurgical and microstructural properties.

Surface roughness and topography of mating surfaces belong to the micro-geometrical paring properties, while load, sliding speed, vibration, shape and dimension of mating surfaces belong to the loading and macro-geometrical properties. The tribochemical properties of the surfaces, such as adsorbed atoms, amount and type of surface films (i.e. oxides), chemical reactivity and thermal conductivity are not independent of environmental properties such as lubricants, humidity, temperature, composition, and partial pressure of gaseous atmosphere. Finally, wear is significantly influenced by the metallurgical properties of the tribosystem which include hardness, work-hardening, crystal structure, crystallographic orientation, ductility and fracture toughness. All these factors work simultaneously in a complex dynamic fashion and, ultimately, determine the type of wear mechanisms taking place.

5.2. Friction

Friction is the resistance to relative motion of contacting bodies. The degree of the resistance to motion is expressed as a coefficient of friction, μ,

$$\mu = \frac{F_N}{F_T} \tag{5.1}$$

where F_N is the normal load and F_T is the tangential force require to sustain sliding.

The value of the coefficient of friction is determined by the sum of the individual contributions of the principal friction components [51]; namely, adhesion (μ_s), ploughing (μ_{pl}) and deformation (μ_d). Hence,

$$\mu = f_a\mu_a + f_{pl}\mu_{pl} + f_d\mu_d \tag{5.2}$$

where the coefficients f_a, f_{pl} and f_d indicate the relative contribution of each component. The actual values of the contributions are determined by the characteristics of the wear mechanisms taking place, which is a function of material properties, and environmental and testing conditions. Many investigators attempted to model friction, however, there is, as yet, no comprehensive model of predicting the coefficient of friction [52].

5.3. Sliding Wear

Sliding wear is defined as the continuous (unidirectional or reciprocating) relative motion between two moving bodies in contact under load. Two modes of sliding wear can be identified; these are termed severe and mild. Severe wear is associated with high wear rates and high coefficients friction and occurs under conditions of high velocities, loads and temperatures. Mild wear usually occurs at low loads and low velocities and is associated with lower wear rates and lower coefficients of friction than the severe wear. Sliding wear can be well described by Archard's law of wear [50],

$$W = \frac{KF_n}{H} \tag{5.3}$$

where W is the volume worn per unit sliding distance, F_N is applied load, H is the hardness of the softer materials in contact and K is the wear coefficient. Eq. 5.3 is

valid for either severe or mild wear, but does not predict any transition in the wear rate. During sliding a transition from severe to mild wear is commonly observed. This type of transition known as distance-dependant transition is attributed to a combination of work-hardening, the formation of surface oxides and smoothening out of the initial surface roughness. The last factor is equivalent to gradual, but continuous, reduction in the true contact pressure during sliding, which would result in reduction in the measured rate of wear [53].

There are several possible mechanisms of sliding wear, which are identified based on the type of material removal process taking place. Many different mechanisms of sliding wear are proposed in the literature [50-55]. However, the most commonly cited mechanisms of wear in the literature include abrasion and adhesion.

5.3.1. Abrasion

Abrasion is the most common mechanism of wear and may be described as damage to a surface by a hard material [51]. It is also sometimes called scratching, scoring and gouging depending on the degree of severity. Abrasion covers two general situations. In both situations wear occurs by the removal of material from the softer surface by a harder surface. In the first instance, asperities of a harder material sliding against a softer one (two-body-abrasion). In the second case, abrasion is caused by loose hard particles sliding between rubbing surfaces (three-body-abrasion).

Abrasive wear process occurs by combined effects of microploughing, microcutting and microcracking [56]. In the ideal case, microploughing due to a simple pass one hard asperity does not result in any detachment of material from a surface being worn. The material is usually displaced sideways forming a ridge adjacent to the groove. Material loss can occur by microcrackcing of ridges as a result of repeated passing of the slider on the same wear track. Pure microcutting occurs by cutting of a material ahead of the asperities and result in a formation of a chip equal in volume to the wear groove produced. Microploughing and microcutting are common in ductile materials. The proportion of microploughing to microcutting depends on both the hardness and the attack angle of the asperity (the angle between the asperity and the wearing surface). When the hardness of the harder material is much larger than the

softer one and the attack angle is high, microcutting will dominate resulting in higher wear rates than microploughing.

The shape and the size of wear debris also contribute to the ploughing of the softer surface (three-body-abrasion), especially, when these debris come from the harder surface or from the hard oxide debris forming. The wear rate is expected to be higher for sharp pointed debris (i.e. abrasive particle) than from blunt rounded abrasive. The wear rate also increases as the abrasive particle size increases.

5.3.2. Adhesion

According to early theory of Bowden and Taylor [52], adhesion occurs as a result of relative sliding between two surfaces under a normal contact load. It is assumed that when asperities come into contact, they adhere strongly to each other and form asperity junctions. Continued sliding causes the junctions to be sheared and separation of the surfaces occur in the bulk of the softer material. This process leads to fragments of the softer material adhering to the harder one.

6. FRETTING AND RECIPROCATING SLIDING WEAR

6.1. Fretting Wear

Fretting is the small-amplitude oscillatory movement that may occur between contacting surfaces, which are usually nominally at rest. It results in two forms of damage: surface wear and deterioration of fatigue life. The extent of wear and surface damage is much greater than suggested by the magnitude of sliding distance. Reciprocating movements as short as 0.1 μm in amplitude can cause failure of the component when the sliding is maintained for one million cycles or more [54].

The sequence of events is characterized by:

i. Vibration and sliding.

ii. Adhesive wear and generation of debris.

iii. Oxidation of that debris, which remains trapped in the small contact area.

iv. Abrasion by that debris, with an increased wear rate and even more debris production.

v. It results in significant localized damage and sometimes a runaway situation.

One of immediate consequences of process in normal atmospheric conditions is the production of oxide debris; hence the term fretting wear or fretting corrosion is applied to the phenomenon.

The movement is usually the result of external vibration, but in many cases it is the consequences of one of the members of the contact being subjected to a cyclic stress, which gives rise to another and usually more damaging aspect of fretting, namely the early initiation of fatigue cracks. This is termed fretting fatigue.

The terms fretting and fretting corrosion are now widely accepted in most languages, but the term "reiboxydation" is still used in Germany, and corrosion de trepidation is occasionally used in France [55].

Fretting was first reported by Eden, Rose and Cunnigham in 1911, who found that brown oxide debris was formed in the steel grips of their fatigue machine in contact with a steel specimen [55].

6.1.1. Fretting Wear in Mechanical Components

Because vibration is one of the main causes of the fretting movement, it follows that he most likely area for it to occur is in machinery. The contacts between hubs, shrink- and press-fits, and bearing housings on loaded rotating shafts or axles are particularly prone to fretting damage [57].

Jointed structures are another source of fretting problems. According to Mitchell, there is no such thing as a static joint on an aircraft. An aircraft structure is largely an assemblage of aluminum and steel components riveted together or joined by fasteners. Even in a simple riveted joint, there are at least three possible sites where fretting can occur (Figure 6.1) [54]:

i. Between the rivet panels

ii. Between the under site of the rivet head and the panel

iii. Between the shank of the rivet and the rivet holes

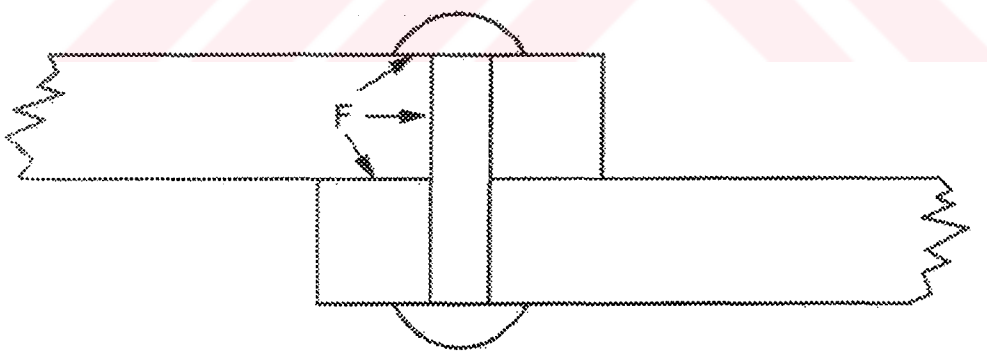

Figure 6.1 Locations (indicated by F) prone to fretting in an aluminum-steel riveted joint [54].

Turbines, both steam and gas, operate under conditions that subject these components to fretting damage. There are three main sites:

i. Where the turbine disk is either shrink-fitted onto driving shaft or attached to the shaft by means of a bolted flange.

ii. Where the blades are fixed into the disk by either a dovetail or fir-tree type fixture.

iii. Where snubbers at the outer ends of the blades contact those on adjacent blades.

The rotors of electrical generators have slots along their lengths in which the windings are located. These are held in place by wedges. Fretting can occur between the wedges and the undercut portion of the winding channel with the development of fatigue cracks in the rotor.

In steam generators and heat exchangers, flow-induced vibration results in fretting between and the supports or baffles through which they pass.

Fretting can occur in certain orthopedic devices, particularly fracture fixation devices such as bone plates. These are used to hold together the parts of fractured bone. They consist of plates of corrosion-resistant materials that are attached to the bone by means of screws of same material. Fretting can occur between the underside of the screw head and the counter sink of the hole in the plate. Fretting in this case results in disruption of otherwise protective films the continual release of heavy metal ions in the body fluid, with possible toxic reactions [55].

6.1.2. Parameters Affecting Fretting

The main parameters affecting the fretting are amplitude of slip, normal load, frequency of vibration and environmental conditions. These parameters are discussed in detail below.

6.1.2.1. Amplitude of Slip

Tomlinson established that relative movement essential for fretting to occur and showed that extremely small movements of the order of a few nanometers were capable of causing damage. One of the problems in experimental work has been the control and measurement of small amplitudes of movement. The most satisfactory method which avoids possible losses due to elastic deformations is to concentrate on the situation of partial slip.

Figure 6.2 shows the form of contact of a ball on a flat developed from the Hertzian solution for a stationary contact. On the application of a tangential force or a torsional

force, slip occurs over an outer annular region of the circle of contact. If the applied force is oscillating, then fretting occurs in the slip region.

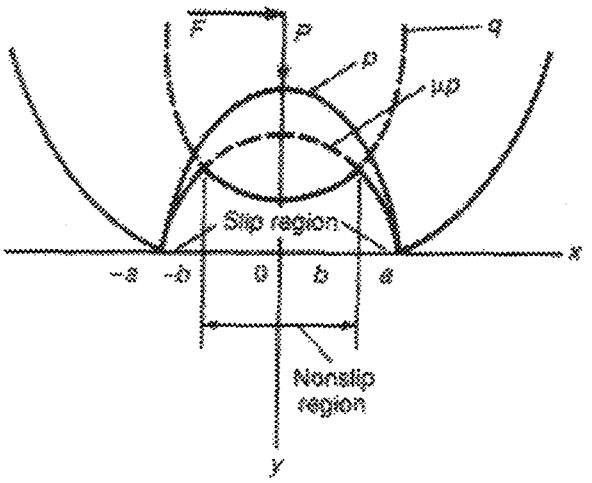

Figure 6.2 Partial slip for a ball in contact with a flat and subjected to a tangential force [55].

As the amplitude was increased, the damage area, characterized by the appearance of the typical reddish-brown oxide, increased in width, with the outer radius remaining constant.

The amplitude of slip where the slip becomes total has been termed the critical amplitude, Δ. In Figure 6.3 the relation between the critical amplitude and normal load is given.

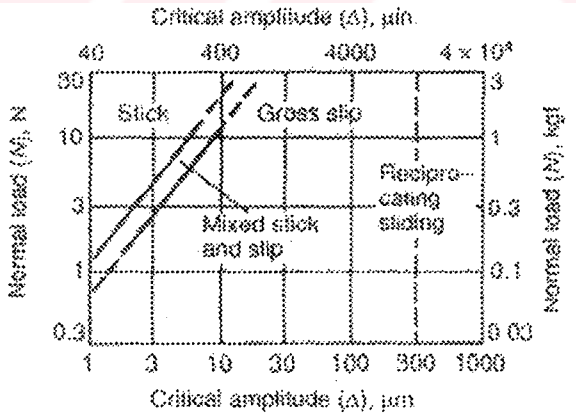

Figure 6.3 Plot of normal load versus critical amplitude as a function normal slip for a crossed steel cylinder arrangement [55].

In other investigations, using a variety of different contact geometries and different methods of assessing the wear rate and plotting the results as the specific wear rate (that is, the loss of material per unit of sliding distance per unit of applied normal load), the curves are of the form shown in Figure 6.4. The curves are sigmoidal,

with the specific wear rate becoming constant at amplitudes > 100 μm (>0.004 in.) (That is, identical with unidirectional sliding or reciprocating sliding wear rates). This then gives a possible upper limit for the slip amplitude for the case of true fretting [55].

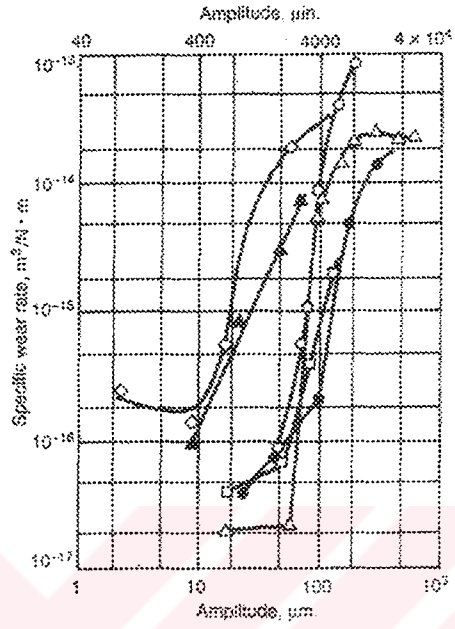

Figure 6.4 Plot of specific wear rate versus amplitude of slip [55].

6.1.2.2. Normal Load

When two surfaces are placed in contact and loaded, plastic deformation of contacting high spots (asperities) occurs. However, certain contacts (for example, sphere on flat and cylinder on flat), where the contact area tends to be extremely small, still conform to the elastic theory of Hertz because the overall contact is determined by the elastic stress field developed in the hinterland or bulk of the material. In most practical cases of contact between conforming surfaces, plastic deformation is to be expected at contacting high points. The real area of contact, A, is therefore directly proportional to the applied load, P:

$$A = \frac{P}{P_0} \tag{6.1}$$

where P_0 is the yield pressure and roughly equal to 3Y, and where Y is the yield stress in tension. Because fretting only occurs at contacting areas, it follows that the amount of wear should be directly proportional to the applied load. This is generally found to be the case if the amplitude of slip is kept constant [55].

6.1.2.3. Frequency

The effect of frequency was originally studied by Uhlig, who found an increase in wear volume at low frequencies for a given number of cycles (Figure 6.5). This was related to the formation and disruption of oxide films [55].

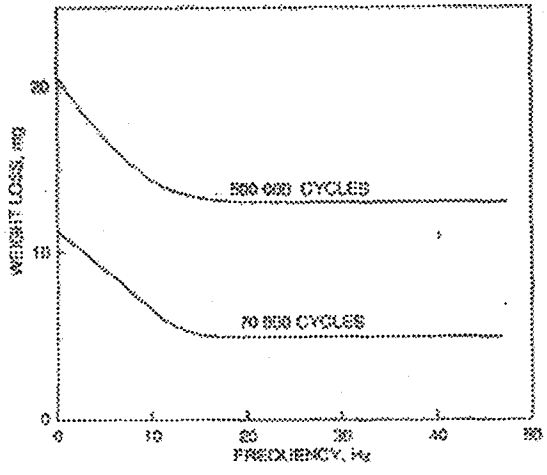

Figure 6.5 Plot of wear versus frequency of fretting vibration [55].

6.1.2.4. Environmental Effects

The most significant environmental factors in fretting are relative humidity and temperature. Wear rate decreases with increasing relative humidity due to the formation of a film which makes it easier to slide. According to result of studies given in literature, wear rate decreases with increasing temperature [55].

6.2. Reciprocating Sliding Wear

Wear mechanisms in fretting change depend on the amplitude of slip (Figure 6.6). At very small amplitudes (less than 1 μm) the wear rate is negligibly small. Under these conditions no microslip occurs in the contact and there is consequently very little damage. As the amplitude is increased, significant microslip develops and the wear rate rises slowly. Once gross slip occurs (at amplitudes greater than 10 μm) a rapid rise in wear rate occurs, which eventually levels off to the constant value expected for reciprocating sliding wear at amplitudes greater than 300 μm [55].

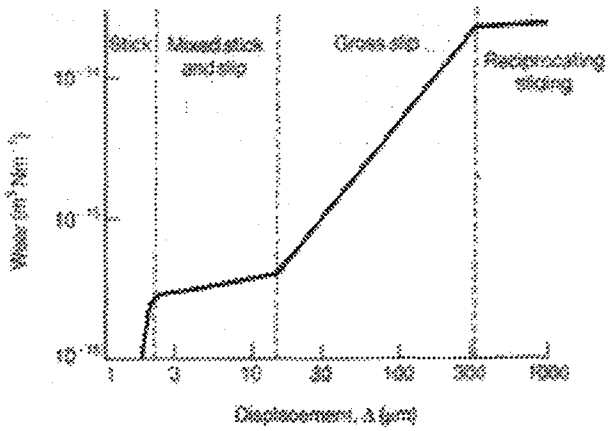

Figure 6.6 The variation of fretting wear with amplitude of slip Δ for a wide range of steel [55].

In reciprocating sliding wear contact area between two mated surfaces has the displacement distance more than amplitude of slip. In the other words, if the material displaces more than its length reciprocating sliding wear occurs [58].

The main characteristics of reciprocating sliding wear are the debris produced is not oxidized within the contact and wear coefficient is greater than under the corresponding fretting conditions [59].

7. EXPERIMENTAL PROCEDURE

In this study, the effects of silver content on mechanical and structural properties of γ-Mo_2N-Ag coatings were investigated. As a substrate material high speed steel (HSS) specimens were used. Phase structure and grain size of coatings were determined by X-ray diffraction analyses. Surface and cross-section morphologies and chemical composition of coatings were determined by scanning electron microscopy and energy dispersive spectrometry. Thickness, roughness, hardness, adhesion property and wear behavior of coatings determined by calotest, profilometer, ultra microhardness, Rockwell C, and reciprocating wear tests, respectively.

7.1. Substrate Preparation

The high speed steel (HSS) specimens which have 20 mm diameter, 5 mm thickness were used as substrate materials in the experiments. The surfaces of the specimens were prepared by standard metallographic techniques. The final polishing was done by with a 1 μm diamond paste. After polishing process, specimens were ultrasonically degreased in hot alkaline baths and then rinsed in deionized water, dried in isopropyl alcohol and immediately loaded into the chamber.

7.2. Deposition of Coatings

A pulsed DC magnetron sputter deposition unit was used as the sputter system in the experiments. The deposition system and procedures are described below.

The films were deposited by physical vapor deposition (PVD) machine (Novatec-SIE, Model: NVT-12) which has an arc PVD cathode and an unbalanced magnetron gun combining with a pulsed DC magnetron power supply. All substrates were pre-heated by arc PVD cathode before deposition process. The applied bias voltages for pre-heating of substrates were -600, -800 and -1000 V each for 2 min. All substrates

were coated by molybdenum interlayer by applying -150 V bias voltage for 2 minutes to increase the adhesion of coatings to the substrate.

The diameter of the Mo target was 63 mm and the purity of the target is 99.99 %. Pre-sputtering of the target was conducted before the deposition to remove any possible contaminations from the target surface. Pre-sputtering was carried out for ten minutes prior to the deposition of γ-Mo_2N and γ-Mo_2N-Ag coatings. The power of pre-sputtering was set at just the same as the deposition condition i.e. 500W. The shutter was closed to prevent contamination of the substrate during the pre-sputtering stage.

After pre-sputtering, substrates moved in front of unbalanced magnetron gun and shutter was opened. For the formation of γ-Mo_2N and γ-Mo_2N-Ag coatings, 70 % argon and 30 % nitrogen was introduced into the chamber. The volume percentage of nitrogen and argon in the total sputtering gas mixture was controlled by flow rate of the individual flowmeter. Different silver contents (0 to 10 at %) in γ-Mo_2N-Ag coatings were obtained through the variation of the diameters of silver spots (0 to 5 mm) on Mo target. All deposition was carried out under the condition of 500 W of power and with infrared (IR) heating of the substrate. During sputtering of γ -Mo_2N and γ-Mo_2N-Ag coatings the substrate temperature were kept about 250°C. The distance between the target and the substrate was maintained at 50 mm during the whole deposition process. Deposition time of γ-Mo_2N and γ-Mo_2N-Ag coatings was 30 min.

The samples deposited with 0, 1, 6 and 10 at % silver content under constant total sputtering gas pressure of $7.5x10^{-3}$ Torr.

7.3. Characterization of Coatings

7.3.1. X-Ray Diffraction Analysis

The crystal structures of the samples deposited under different conditions were determined by the X-ray diffraction (XRD) method (Philips X'pert Cu-Kα) at a voltage of 40 kV and a current of 40 mA. The main characteristics of an X-ray diffraction pattern are the intensity, position, and full width at half maximum. The intensity of a diffraction pattern indicates the quantity and preferred orientation of the phase present in the sample.

The lattice constant, strain and the crystalline size were determined from the peak position and the shape of the diffraction pattern. The lattice parameter of Mo-N coating was calculated from the diffraction angle from XRD data by using Bragg's law:

$$n\lambda = 2d\sin\theta \tag{7.1}$$

where d is the spacing between diffraction planes, λ is the diffraction angle and λ is the wavelength of the Cu-Kα radiation.

The grain size of molybdenum nitride coating with 0%, 1% and 10% Ag content was determined by Scherrer's equation [75].

$$B = \frac{0.9\lambda}{t\cos\theta} \tag{7.2}$$

Here B is the full width half maximum (FWHM) of the diffraction peak in radians obtained by Gaussian curve fitting, t is the diameter of the particle, λ is the wavelength of the Cu-Kα and θ is the diffraction angle.

7.3.2. Energy Dispersive Spectrometry (EDS) Analysis

The silver content in the Mo_2N-Ag coatings was determined by using a NORAN 2100 Freedom EDS analyzer equipped in Jeol JSM-5410 model scanning electron microscope and Voyager analysis system. Analyses were taken from different positions on specimens for determining the homogeneity of coatings. Only metallic content of the coatings were taken into account in chemical composition analyses and nitrogen content was excluded.

7.3.3. Thickness Measurement

The thickness of the coatings was measured by Eifeler Nord Coating Caloprep thickness measurement device. Calotest provides quick, simple and inexpensive determination of coating thicknesses. A rotating sphere with a know diameter (Ø ball) is pressed on the coating surface with a pre-selected load. Both the position of the sphere relative to the sample and the contact load are constant. Upon adding abrasive paste to the contact zone, a depression with the shape of a spherical cap is abraded into both the coating and the substrate.

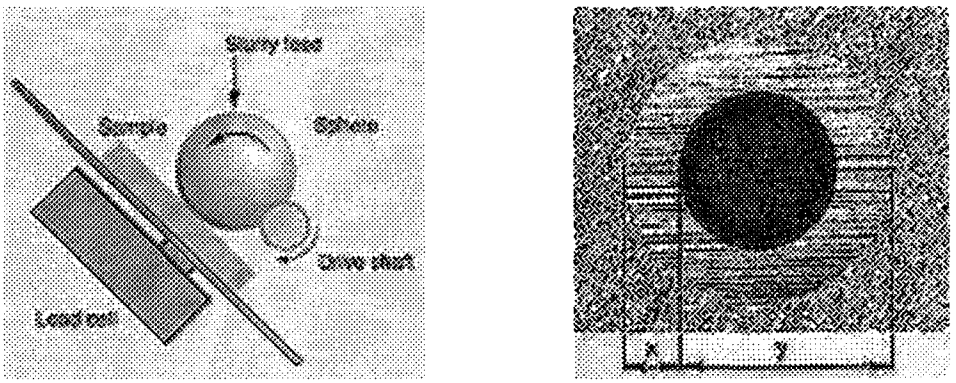

(a) (b)

Figure 7.1 (a) Schematic representation of calotest (b) optical microscope image of wear crater [60].

Optical inspection of the depression reveals the projected surfaces of the abraded coating and substrate sections (Figure 7.1.b). By measuring the parameters X and Y, the thickness of the coating, D can be calculated by a simple geometrical equation (Eq, 7.3).

$$D = \frac{XY}{\Phi_{ball}} \tag{7.3}$$

7.3.4. Hardness Measurement

Hardness measurements were conducted by a dynamic ultra microhardness tester (Fischerscope H 100 XYPROG) equipped with an elongated Vickers type indenter. Ultra microhardness tester has the ability of applying load in pre-defined steps and time intervals. In homogeneous materials hardness is independent of indentation depth. However, while indenter penetrates into the coating energy accumulation around the indenter forms a spherical artificial tip. In coating systems, when depth of penetration exceeds the 1/10 to 1/7 of coating thickness this artificial tip will reach to substrate material and apply a load like real tip. Thus, the hardness value of the coating won't be measured correctly. The hardness of coating usually measured lower than its correct value because of low hardness of substrate material. Therefore, appropriate load was selected to prevent the indenter penetrates deeper than 1/10 to 1/7 of the coating. Hardness values can vary with the applied loads when the applied loads were low. Thus, a total load of 100 mN was selected dependent upon coating thicknesses and applied in 120 steps with a time interval of 0.5 s at each step. Each measurement was repeated at least 25 times for an average hardness value. After

measurements results were evaluated with Fischer H100V-HCU Version 1.6 software to obtain average values of hardness and elastic modulus.

7.3.5. Roughness Measurement

The surface roughness of specimens before and after deposition process was measured by Mahr Perthen Perthometer S8P surface profilometer equipped with Focodyn optical probe. Average roughness value was taken into account and measurement parameters were LT: 1.750 and VB: 62.5. Average roughness value can be defined arithmetical average of whole roughness area (DIN 4762, DIN 4768 and ISO 4287/1). Although, average roughness value does not give an opinion about surface profile, it is most widely used parameter to determine the surface roughness value.

7.3.6. Microstructure Investigations

The surfaces and the cross-section morphologies of coatings were examined with a Jeol JSM-5410 scanning electronic microscope (SEM). HSS specimens which have thickness of 1 mm were used in cross-section investigations. In this experiment, changes in growth morphologies of Mo_2N and Mo_2N-Ag coatings with different Ag contents were investigated and zone models of coatings were determined.

7.3.7. Adhesion Properties

Investigation of adhesion of coatings to the substrate material was made by means of Rockwell C test. Rockwell C adhesion test is a method of checking the adhesion of PVD coatings that relies on observation of a Rockwell C indent. The stresses around the rim of a normal Rockwell C indent can cause microcracking and delamination of the coating. Because these stresses are greatest at the rim of the crater and then taper off radially outward, the size of the affected area gives an indication of the adhesion of the coating.

7.3.8. Wear Properties

Investigations of the wear properties of coatings were conducted by Plint & Partners TE 70 Micro Friction device. Parameters used in the experiments were given in Table 7.1.

Table 7.1 Parameters of fretting wear experiments

Frequency (Hz)	50±0.02
Amplitude of Slip (μm)	1000±2
Time (min)	60
Load (N)	5
Humidity	40 %
Temperature (°C)	28

In the experiments M50 tool steel balls with 10 mm diameter were used as counterbody. Chemical composition and mechanical properties of M50 tool steel balls are given in Table 7.2.

Table 7.2 Chemical composition and mechanical properties of M50 tool steel balls.

Chemical Composition				**Mechanical Properties**	
C	0.77-0.85 % max	**Ni**	0.15 max	**Hardness**	60-65 Rc
Mn	0.35 % max	**V**	0.90-1.10	**Max. Operating Temp.**	480 °C
Si	0.75 % max	**Mo**	4.00-4.50	**Density**	7.972 g cm^{-3}
P	0.015 % max	**Co**	0.25 max		
S	0.015 % max	**W**	0.25 max		
Cr	3.75-4.25 % max	**Cu**	0.10 max		

After reciprocating wear tests all specimens were examined with Jeol JSM-5410 scanning electronic microscope. Wear volume (V) of M50 tool steel balls were calculated from the equation (7.4).

$$V = \frac{\pi d^4}{64r} \tag{7.4}$$

where D is the diameter of the wear scar and r is the radius of the ball.

8. RESULTS

8.1. Crystal Structures

The XRD spectra of the γ-Mo_2N and γ-Mo_2N-Ag thin films deposited on HSS substrates at different silver contents are shown in Figure 8.1. As shown in the XRD spectra, with increasing silver content increased, the intensity of γ-Mo_2N peaks decreased, indicating a decrease in the crystallinity of the molybdenum nitride thin film.

The results of the XRD studies on various γ-Mo_2N-Ag coatings which were deposited with different silver content (0, 1, 6 and 10 at %) are shown in Figure 8.1. Figure 8.1 shows that XRD pattern of the film without silver content was consistent with the JCPDS card of γ-Mo_2N phase. The JCPDS card of γ-Mo_2N is given in Table 8.2 [36]. The most intensive diffraction peak belonged to (200) plane at diffraction angle of 43.149°. Other intensive peaks in diffraction pattern exhibited that the film is not preferentially orientated. Films had diffraction peaks belonging to (111), (200), (220), (311), (222), (331) and (420) planes. Addition of silver content increased the intensities of diffraction peak from (200) plane and decreased the intensities of diffraction peak arousing from other planes. Besides, the intensity of diffraction peak of (110) plane of Mo phase in γ-Mo_2N thin film decreased and this diffraction peak disappeared with the increase of Ag content. It is also shown in Figure 8.1 the diffraction angle of diffraction angles of γ-Mo_2N peaks continuously shifted to lower angle direction.

In the diffraction patterns of γ-Mo_2N-Ag thin films (Figure 8.2) it is shown that the diffraction peaks of γ-Mo_2N continuously shifted to lower diffraction angles and as the silver content in the films increased the diffraction peaks of γ-Mo_2N shifted to their original positions given in JCPDS cards. There was no silver phase observed in γ-Mo_2N-Ag thin films as shown in Figure 8.1. The absence of silver phase in the diffraction patterns suggested that silver was either in amorphous or in nanocrystalline structure. The JCPDS card of Ag is given in Table 8.2 [36].

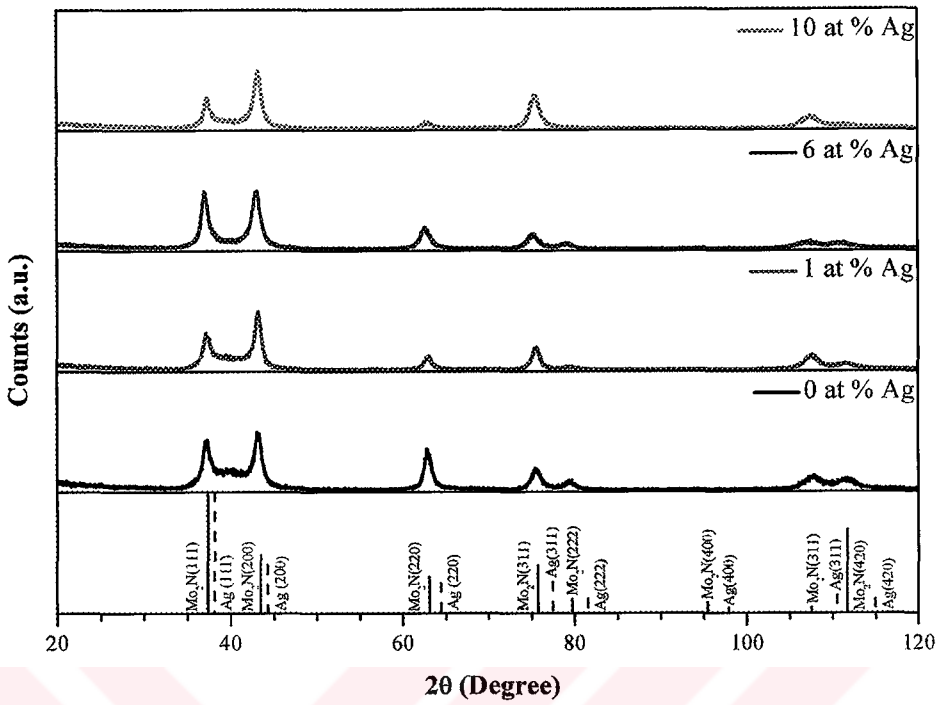

Figure 8.1 XRD spectra of γ-Mo_2N and γ-Mo_2N-Ag thin films sputtering deposited with different silver contents

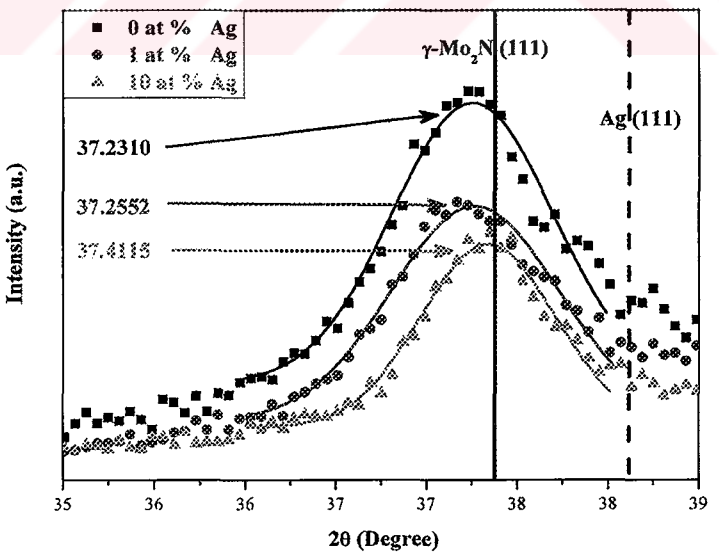

Figure 8.2 Shifts in diffraction peaks of γ-Mo_2N and γ-Mo_2N-Ag coatings.

Table 8.1 JCPDS card of γ-Mo_2N [36].

Card No: **25-1366**	**2θ**	**Intensity**	**h k l**
γ - Mo_2N	37.376	100	1 1 1
	43.450	48	2 0 0
Cu-Kα (λ = 1.54056 Å)	63.106	30	2 2 0
	75.725	40	3 1 1
Cubic	79.708	12	2 2 2
a = 4.1630 Å	95.453	9	4 0 0
	107.525	5	3 3 1
	111.659	69	4 2 0

Table 8.2 JCPDS card of Ag [36].

Card No: **04-0783**	**2θ**	**Intensity**	**h k l**
Ag	38.117	100	1 1 1
	44.279	40	2 0 0
Cu-Kα (λ = 1.54056 Å)	64.428	25	2 2 0
	77.475	26	3 1 1
Cubic	81.539	12	2 2 2
a = 4.0862 Å	97.891	4	4 0 0
	110.501	15	3 3 1
	114.928	12	4 2 0
	134.890	13	4 2 2

Table 8.3 shows the grain sizes and the lattice constants of γ-Mo_2N and γ-Mo_2N-Ag coatings were calculated from the XRD patterns. As shown in Table 8.3, the lattice constant calculated from Bragg's equation is 4.1708 Å for γ-Mo_2N, which were larger than the JCPDS value of 4.1630 Å for fcc γ-Mo_2N [37]. With increasing silver contents, the lattice constant of γ-Mo_2N slightly changed to 4.1689, 4.1859 and 4.1708 Å.

The grain sizes of γ-Mo_2N and γ-Mo_2N-Ag coatings with 0% to 10% silver content were calculated from Scherrer's equation (7.2) using full width at half maximum (FWHM) of the diffraction peak of (111) plane, under the assumption that strains are not contributing to the peak broadening, are also shown in Table 8.3. The particle sizes in the thin film slightly decreased with the increase in the silver content.

Table 8.3 Lattice constants and grain sizes of γ-Mo_2N and γ-Mo_2N -Ag thin films

Silver Content (%)	Lattice Parameter (Å)	Grain Size (nm)
0	4.1708	16.96
1	4.1689	16.40
6	4.1859	15.17
10	4.1708	14.51

8.2. Energy Dispersive Spectrometry (EDS) Analysis

Chemical compositions of γ-Mo_2N and γ-Mo_2N-Ag coatings were determined only for metallic content by energy dispersive spectrometry analyses are given in Table 8.4. Silver contents of γ-Mo_2N-Ag coatings were determined as 0, 1.08, 5.92 and 9.89 at % and represented as 0, 1, 6 and 10 at % in the text respectively. Chemical compositions of coatings were consistent with pre-calculated values according to the area ratio of each element taking into account their sputtering yields.

Table 8.4 EDS analysis of γ-Mo_2N and γ-Mo_2N-Ag thin films

Coating	EDS			
	Mo		Ag	
	at %	wt %	at %	wt %
γ-Mo_2N	100	100	0	0
γ-Mo_2N-Ag	98.92	98.79	1.08	1.21
γ-Mo_2N-Ag	94.08	93.42	5.92	6.58
γ-Mo_2N-Ag	90.11	89.02	9.89	10.98

8.3. Thickness Measurements

Thicknesses of as deposited thin films are given in Table 8.5. As shown in Table 8.5 coating thicknesses are about 7.5μm and silver content in the film has no appreciable effect on coating thickness.

Table 8.5 Thicknesses of γ-Mo_2N and γ-Mo_2N-Ag thin films

Silver Content (%)	Thickness (μm)
0	7.83
1	7.56
6	7.68
10	7.73

8.4. Hardness Measurements

The dependency of the microhardness of γ-Mo_2N and γ-Mo_2N-Ag coatings as a function of Ag content is given in Table 8.6. Table 8.6 shows that microhardness of γ-Mo_2N-Ag coatings increased to a maximum value and then decreased with increasing of Ag content. The maximum microhardness value obtained from 1 at % Ag containing γ-Mo_2N-Ag coating was 3430±25 kg mm^{-2} (33±0.25 GPa). The microhardness of γ-Mo_2N coatings were increased from 2860±15 kg mm^{-2} (28±0.15 GPa) up to 3430±25 kg mm^{-2} (33±0.25 GPa).

In Table 8.6 elastic modulus of γ-Mo_2N and γ-Mo_2N-Ag coatings are also given. Elastic modulus of γ-Mo_2N and γ-Mo_2N-Ag coatings increased to a maximum value and then decreased with increasing of Ag content. The maximum elastic modulus value obtained from 1 at % Ag containing γ-Mo_2N-Ag coating was 375±1.47 GPa. The elastic modulus of γ-Mo_2N-Ag coatings with 6 and 10 at % Ag content were lower than the elastic modulus of γ-Mo_2N coating.

.

Table 8.6 Hardness and elastic modulus of γ-Mo_2N and γ-Mo_2N-Ag thin films

Silver Content (at %)	Hardness (kg mm^{-2})	Hardness (GPa)	$E/(1-v^2)$ (GPa)
0	2860±15	28±0.15	375±1.47
1	3430±25	33±0.25	390±2.61
6	3100±27	30±0.26	335±1.91
10	3130±17	31±0.18	340±1.64

8.5. Roughness

Surface roughness of uncoated and coated substrates is given in Table 8.7. In Table 8.7 it is shown that surface roughness of thin films increases with increasing silver content.

Table 8.7 Surface roughness of specimens before and after deposition

Silver Content (%)	Surface Roughness Before Coating (μm)	Surface Roughness After Coating (μm)
0	0.06	0.25
1	0.06	0.48
6	0.06	0.50
10	0.06	0.54

8.6. Microstructure Investigations

The silver content has significant influence on both the surface morphologies and fracture cross-section structures of the as-deposited thin films. Figure 8.3 and Figure 8.4 are the surface morphologies and the cross section structures of the thin films deposited with different silver contents. As shown in Figure 8.3 the surface roughness of the film increases as the silver content in the film increases.

As shown in Figure 8.4 the microstructure of the films change from a dense columnar one (Figure 8.4(a)), through featureless one (Figure 8.4(c)). As expected, the films with high hardness values exhibit a very dense fibrous microstructure such 1% silver containing γ-Mo_2N-Ag coating. (Figure 8.4(b)) It is thought that silver occupies the defected sites in the crystal structure such as grain boundaries. Thus, silver can hinder grain growth and decrease the grain size of γ-Mo_2N phase. As a result at 10% silver content γ-Mo_2N-Ag coating has featureless structure. (Figure 8.4(c))

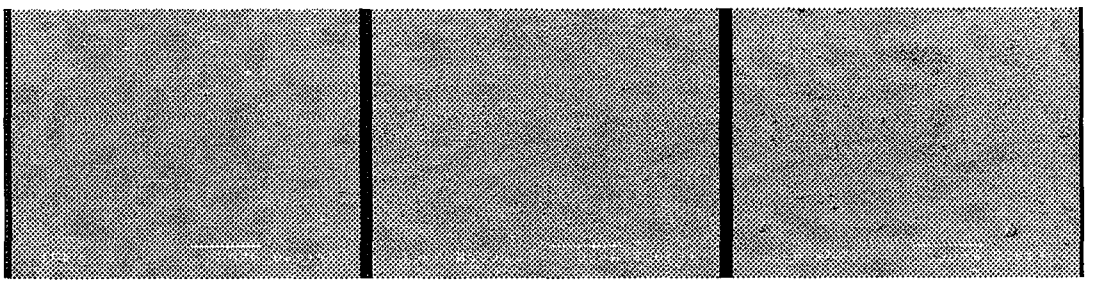

(a) (b) (c)

Figure 8.3 SEM surface morphologies of as-deposited γ-Mo_2N and γ-Mo_2N-Ag thin films with different silver contents (a) γ-Mo_2N (b) γ-Mo_2N-Ag with 1% silver content (c) γ-Mo_2N-Ag 10% silver content

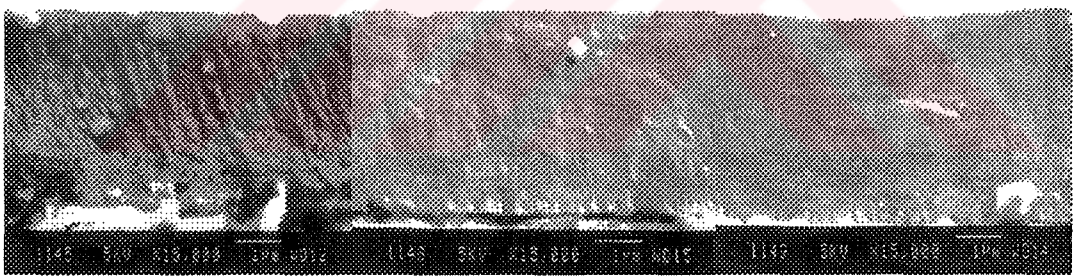

(a) (b) (c)

Figure 8.4 SEM cross sections of as-deposited γ-Mo_2N and γ-Mo_2N-Ag thin films with different silver contents (a) γ-Mo_2N (b) γ-Mo_2N-Ag with 1% silver content (c) γ-Mo_2N-Ag 10% silver content

8.7. Adhesion Properties

Rockwell C examinations of γ-Mo_2N and γ-Mo_2N-Ag coatings are given in Figure 8.5 and Figure 8.6. In the Figure 8.5 it is shown that smaller crater diameter is belonging to 1 at % Ag containing γ-Mo_2N-Ag coating. This result is consistent with hardness measurements. As shown in Figure 8.5 none of the coatings peeled form the substrate surface but in areas where stress concentrations increase cracking and chipping of the films were observed.

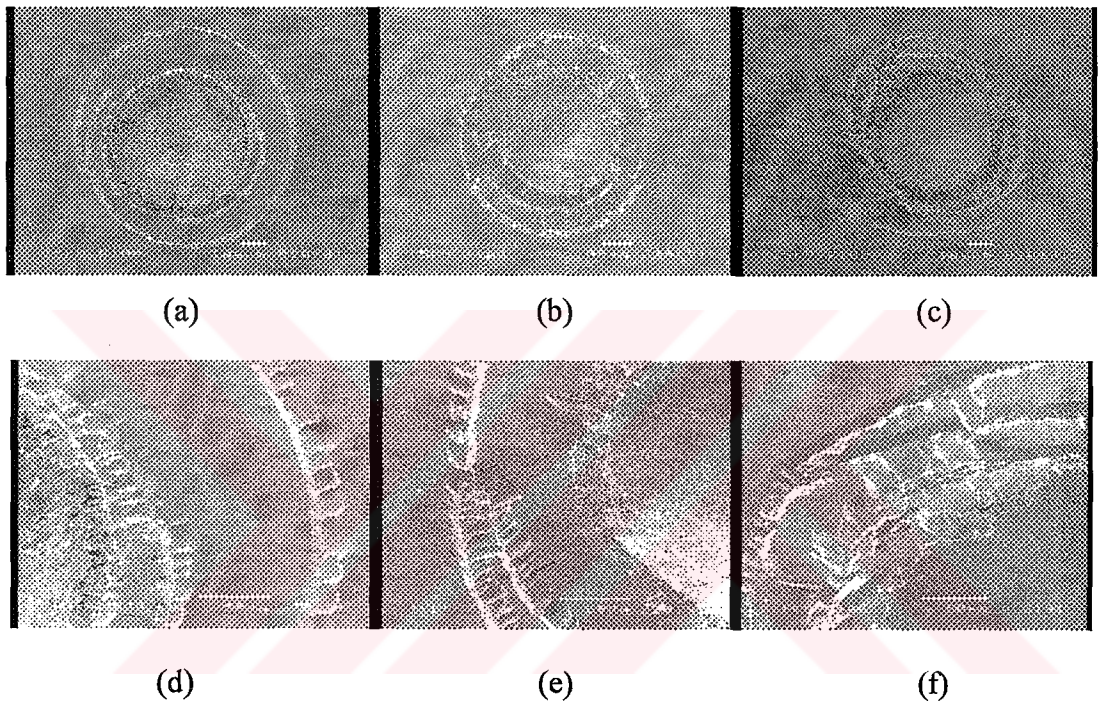

Figure 8.5 Rockwell C indentations of as-deposited γ-Mo_2N and γ-Mo_2N-Ag coatings with different silver contents (a) and (d) γ-Mo_2N (b) and (e) γ-Mo_2N-Ag with 1% silver content (c) and (f) γ-Mo_2N-Ag with 10% silver content.

8.7. Wear Properties

Friction coefficient-distance graphs of γ-Mo_2N and γ-Mo_2N-Ag coatings are given in Figure 8.6. In Figure 8.6 it is shown that γ-Mo_2N coating had the average friction coefficient of 0.79 and γ-Mo_2N-Ag coatings with 1, 6 and 10 at % silver had friction coefficients 0.89, 0.78 and 0.94 respectively.

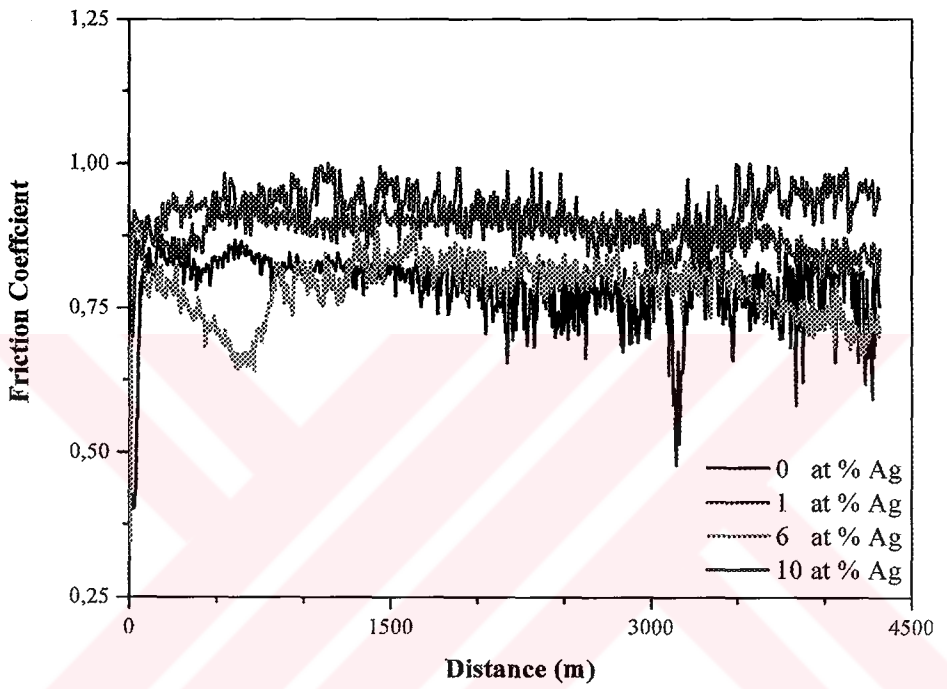

Figure 8.6 Friction coefficient-distance graphs of γ-Mo_2N and γ-Mo_2N-Ag coatings.

Scanning electron microscope images of wear scars on M50 tool steel balls and γ-Mo_2N and γ-Mo_2N-Ag coatings are given in Figure 8.7. Only Fe found in energy dispersive spectrometry analyses taken from wear debris on balls and coatings. The widest wear scars were on γ-Mo_2N-Ag coatings with 1 at % silver content and its counterbody M50 tool steel ball.

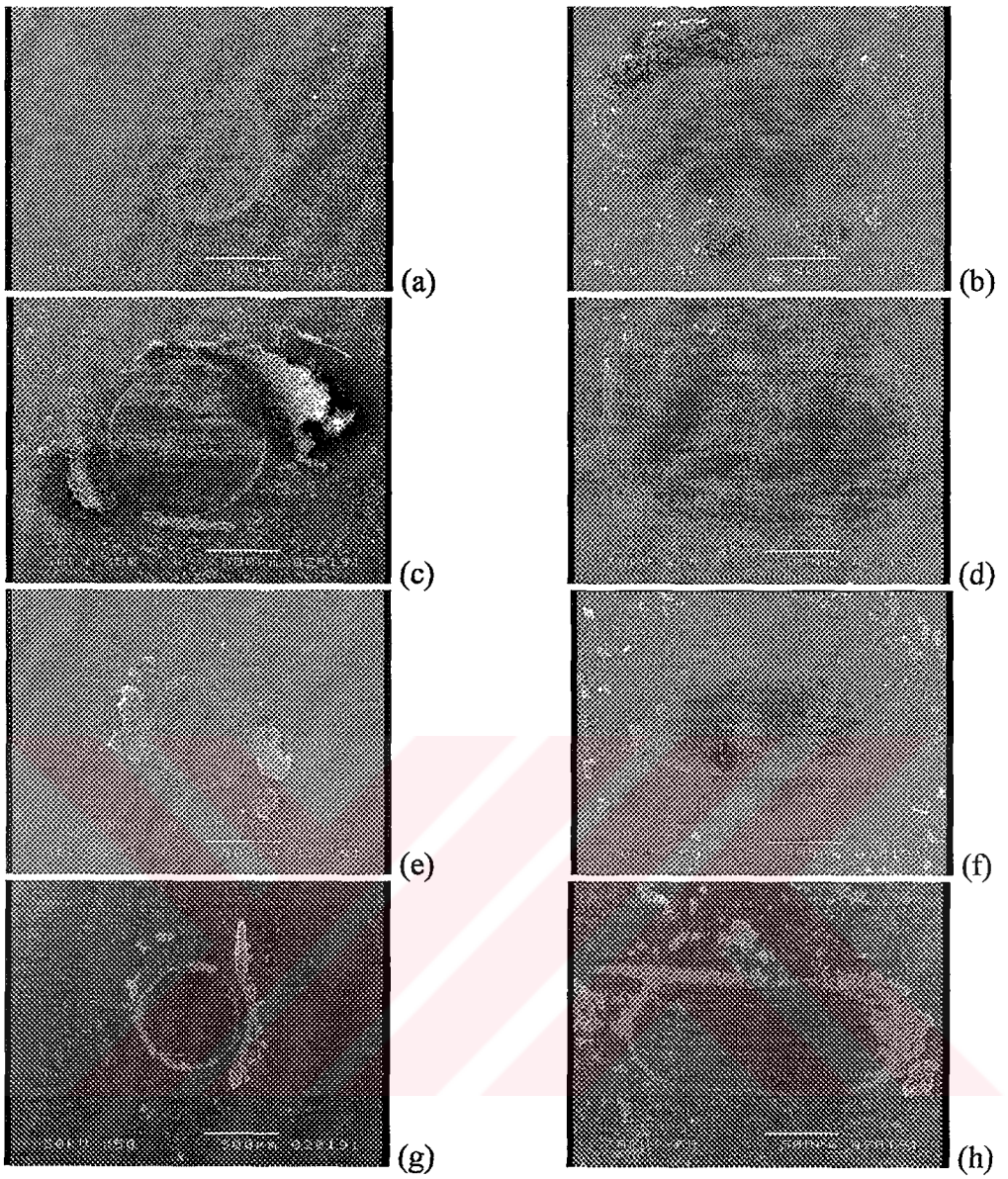

Figure 8.7 Scanning electron microscope images of wear scars on M50 balls and γ-Mo_2N and γ-Mo_2N-Ag coatings. (a) and (b) γ-Mo_2N coating, (c) and (d) γ-Mo_2N-Ag coating with 1 at % silver content, (e) and (g) γ-Mo_2N-Ag coating with 6 at % silver content and (g) and (h) γ-Mo_2N-Ag coating with 10 at % silver content.

Wear volumes of M50 tool steel balls calculated from Equation 7.4 are given in Table 8.8. In Table 8.8, the maximum wear volume belonged to M50 tool steel ball which was counterbody of γ-Mo_2N-Ag coating with 1 at % Ag content. In Table 8.8 widths of wear scars on γ-Mo_2N and γ-Mo_2N-Ag coatings are also given. The widest wear scar belonged to γ-Mo_2N-Ag coating with 1 at % Ag content. Depths of wear scars are an important parameter and they could not be measured in the experiments.

Table 8.8 Wear volumes of M50 tool steel balls and width of wear scars on γ-Mo_2N and γ-Mo_2N-Ag coatings.

Silver Content (at %)	**Average Diameter of Wear Scar on Balls (μm)**	**Widths of Wear Scars on Coatings (μm)**	**Ball Radius (mm)**	**Wear Volumes of Balls ($x10^{-3}$ mm^3)**
0	869.5	950	5	5.61
1	1049	1037	5	11.9
6	747.5	732	5	3.06
10	707	740	5	2.45

9. DISCUSSION

γ-Mo_2N-Ag nanocomposite coatings with different silver contents were produced by magnetron sputtering. In all experiments the parameters, which can be affect the crystal structure of deposited thin films, were kept constant and only the effect of silver content incorporated into the film structure were investigated.

In the diffraction patterns of the thin films (Figure 8.1) it is shown that the diffraction peaks of γ-Mo_2N continuously shifted to lower diffraction angles and as the silver content in the films increased the diffraction peaks of γ-Mo_2N shifted to their original positions given in JCPDS cards (Figure 8.2). Musil report that grain boundaries prevent the formation of dislocations and decrease the internal stresses in the structure when the grain size is smaller than 10 nm [19].He report that TiN peak from (111) plane shifts its original position in 12 at % copper containing Ti-Cu-N coatings nanocomposite coatings compared to 1.5 at % copper containing Ti-Cu-N nanocomposite coatings TiN coatings and thought that it is the indication of compressive stress reduction [48]. Eryılmaz report that grain sizes and internal stresses in the thin films decrease as the copper content in the thin film increases [2]. Thus approaching of diffraction peaks to their original positions of γ-Mo_2N phase is thought to be caused by the decrease of the internal stresses in the films as Ag content increases.

Mo peak appears in γ-Mo_2N coating disappears in γ-Mo_2N-Ag nanocomposite coatings with the increase of silver content. But this situation could not explain.

Incorporation of silver in the film structure decreases grain size of γ-Mo_2N phase and prevents the coating from preferentially oriented due to the favoring of grain growth on other planes.

In the energy dispersive spectrometry analysis silver found in γ-Mo_2N-Ag coatings but in the diffraction patterns of the coatings no silver peak was observed. This means silver was either in amorphous or in nanocrystalline structure.

The cross section structure shows a relationship with silver content. Cross section investigations show that γ-Mo_2N coating has dense and columnar structure that confirms with Zone II structure in Barna and Adamik structure zone model [33].

Incorporation of impurities and additional elements into the coating structure has important effect on zone models. Impurities and additional elements prevent grain growth and favor the nucleation. This causes growth of grains spherically [33]. Columnar structure in γ-Mo_2N coating disappears with increasing silver content in γ-Mo_2N-Ag nanocomposite coatings as seen in Figure 8.4. According to above mentioned and XRD patterns it is seen that increasing of silver content in coatings causes slightly decreasing of grain sizes and growth of grains spherically.

As the silver content in thin film increases, the hardness of the coatings increases to a maximum value and decreases with increasing amount of grain boundaries.

The maximum hardness value is obtained from γ-Mo_2N-Ag nanocomposite coating containing 1% Ag. The hardness of this coating is 3430±25 kg mm^{-2} (33 GPa) under load of 100 mN. Hardness of coatings increases up to 1% silver content and then decreases. Silver content in the film structure has significant effect on hardness. First microhardness increases with decreasing grain size with increasing Ag content and after reaching a maximum value due to reverse Hall-Petch effect microhardness decreases with decreasing grain size with increasing Ag content.

Studies on copper containing nanocomposite coatings, as a similar nanocomposite system, showed that maximum hardness values obtained from 1-2 at % copper containing coatings. Zr-Cu-N nanocomposite coatings have maximum hardness value of 49 GPa with Cu content between 1 and 2 at % [49]. Cr-Cu-N nanocomposite coatings have maximum hardness value of 35 GPa with Cu content of 1 at % [50]. TiN-Cu nanocomposite coatings have maximum hardness value of 30 GPa with silver content of 1.5% [48]. Al-Cu-N nanocomposite coatings have maximum hardness value of 47 GPa at grain size of 9.5 nm with silver content of 8 at % [7].

γ-Mo_2N coating without silver content has columnar structure is clearly seen in Figure 8.4(a). Figure 8.4(b) shows that cross section image of 1% silver containing γ-Mo_2N-Ag coating with the maximum hardness value of 3430.7±25.4 kg mm^{-2} (33 GPa) has dense and columnar structure. In the cross section image of γ-Mo_2N-Ag coating containing 10% silver columnar structure completely disappears. (Figure

8.4(c)) As expected, the films with high hardness values exhibit a very dense fibrous microstructure. Musil report that Zr-Cu-N coating with very high hardness value of 55 GPa has columnar structure and the coatings with high copper containing coatings with the hardness value of 23 GPa has dense structure without columnar growth [49, 51].

In Figure 8.5 it is shown that smallest crater diameter is belonging to γ-Mo_2-Ag thin film with 1% silver content and it confirms that the hardest coating in the experiments. In Rockwell test when the load released there is recovery in substrate. During this recovery cracks which are perpendicular to the surface enlarge. γ-Mo_2N and γ-Mo_2N-Ag coatings have dense columnar and spherical structures as mentioned. In a columnar structure weak regions are grain boundaries. Coatings in dense structures or structure without columns have isotropic behavior like toughness. Detailed investigations of crack regions showed that only 1% silver containing γ-Mo_2N-Ag coating cracked and chipped but not peeled from the surface. As a result the adhesion of γ-Mo_2N-Ag coating the substrate is said to be satisfactory.

Figure 8.6 shows that γ-Mo_2N-Ag coating with 1 and 6 at % silver content has greater coefficient of friction than γ-Mo_2N coating. After 10 at % silver incorporated into the film the friction coefficient of γ-Mo_2N-Ag coatings decreased to a value of 0.78 which was almost the same as friction coefficient of γ-Mo_2N coating.

Studies on silver containing nanocomposite coatings, as a similar nanocomposite system, showed that minimum friction coefficient values obtained from coatings with more 10 at % silver content. In the study of Endrino et al., friction coefficient of TiC-Ag coatings significantly reduced to 0.21 for silver contents more than 10 at % [48]. Another study of Endrino et al. showed that there is a value of silver content for which the tribological properties of these films are optimum. For the films examined, the optimum value for relative silver content is 21 at % for WC–Ag films and 51 at % for TiC–Ag and friction coefficients of 0.25 and 0.26 were obtained respectively [9]. As a result silver content under 10 at % has no significant effect on friction coefficient.

Only Fe found in energy dispersive spectrometry analyses taken from wear debris on M50 tool steel balls. This means that the only M50 tool steel balls were worn. This result was consistent with the surface profilometer results. In the surface profilometer there was no wear depth on γ-Mo_2N and γ-Mo_2N-Ag coatings measured. But wear

depth is very important parameter which must be taken into account to make an interpretation about wear properties of γ-Mo_2N and γ-Mo_2N-Ag coatings.

Table 8.8 also shows the wear volumes of M50 tool steel balls. The maximum wear volume belonged to M50 tool steel ball which was counterbody of γ-Mo_2N-Ag coating with 1 at % Ag content. This result is appreciable because γ-Mo_2N-Ag coating with 1 at % Ag content is the hardest coating in the experiments. Wear volume of counterbody of γ-Mo_2N-Ag coatings with 6 and 10 at % Ag content were smaller than wear volume of counterbody of γ-Mo_2N coating due to the lubricating property of silver. As a result incorporation of sufficient amount of silver into the γ-Mo_2N coating improved the wear behavior of γ-Mo_2N-Ag coatings.

It is also seen from Table 8.8 there no strong relationship between friction coefficient and wear volume.

10. CONCLUSIONS

1. γ-Mo_2N-Ag nanocomposite thin films on HSS substrates were prepared by magnetron sputtering by incorporation of silver into γ-Mo_2N phase.
2. The silver has significant influence on the crystallinity of as deposited thin films. The crystallinity of as deposited thin films decreases with increasing silver content.
3. Silver content has no significant influences on crystal structures of thin film. Under these deposition conditions γ-Mo_2N was the only phase presenting in the coatings.
4. The diffraction peaks of γ-Mo_2N shifted to their original positions given in JCPDS cards as the silver content in the films increased.
5. γ-Mo_2N thin film has columnar structure and it turns into the featureless structure in γ-Mo_2N-Ag nanocomposite thin films as silver content increases.
6. γ-Mo_2N-Ag nanocomposite thin films have smaller grain sizes than MoN thin films. Grain sizes of γ-Mo_2N-Ag nanocomposite thin films sligthly decreases with increasing amount of silver from 17 to 14 nm.
7. The surface roughness of molybdenum nitride thin film increases with the increase of silver content.
8. The maximum hardness value is obtained from γ-Mo_2N-Ag nanocomposite thin film which contains 1% Ag. This hardness value of 3430 kg mm^{-2} (33 GPa) is greater than the hardness γ-Mo_2N thin film.
9. Adhesion properties of γ-Mo_2N-Ag thin films are satisfactory because peeling from the substrate did not occur.
10. Silver content slightly changes the friction coefficients of γ-Mo_2N-Ag coatings between 0.78-0.94.

11. The wear properties of γ-Mo_2N-Ag coatings better than the wear properties of γ-Mo_2N coating. Addition of silver into the γ-Mo_2N coating improved the wear properties.

REFERENCES

[1] **Eryılmaz, O.L.**, 2001. Production and Characterization of Mo-N-Cu Nanocomposite Coatings by Arc Physical Vapor Deposition Technique, *Ph. D. Thesis,* I.T.U. Institute of Science and Technology, Istanbul.

[2] **Veprek, S., Reiprich, S.,** 1995. A Concept for the Novel Superhard Coatings, *Thin Solid Films*, **268**, 64-71.

[3] **Musil, J.,** 2000. Hard and Superhard Nanocomposite Coatings, *Surface and Coatings Technology*, **125**, 322-330.

[4] **Veprek, S.,**1997. Conventional and New Approaches towards the Design of Novel Superhard Materials, *Surface and Coatings Technolgy*, **97**, 15-22.

[5] **Veprek, S.,**1997. The Search for Novel Superhard Materials, *Journal of Vacuum Science and Technology,* **A17**, 2401-2420.

[6] **Musil, J., Hruby, H., Zeman, P., Zeman, H., Cerstvy, R., Mayrhofer, P.H., Mitterer, C.,** 2001. Hard and Superhard Nanocomposite Al-Cu-N Films Prepared by Magnetron Sputtering, *Surface and Coatings Technology*, **142-144**, 603-609.

[7] **Ürgen, M., Eryilmaz, O.L., Çakır A.F., Kayalı, E.S., Nilüfer, B., Işık, Y.,** 1997. Characterization of Molybdenum Nitride Coatings Produced by Arc-PVD Technique, *Surface and Coatings Technology*, **94-95**, 501-506.

[8] **Kazmanlı, M.K., Ürgen, M., Çakır, A.F.,** 2003. Effect of Nitrogen Pressure, Bias Voltage and Substrate Temperature on yhe Phase Sturucture of Molybdenum Nitride Coatings Produced by Cathodic Arc PVD, *Surface and Coatings Technology*, **167**, 77-82.

[9] **Endrino, J.L., Nainaparampil, J.J., Krzanowskia, J.E.,** 2002. Magnetron Sputter Deposition of WC–Ag and TiC–Ag Coatings and Their Frictional Properties in Vacuum Environments, *Scripta Materialia*, **47**, 613-618.

[10] **De los Arcos, T., Oelhafen, P., Aebi, U., Hefti, A., Duggelin, M., Mathys, D., Guggenheim, R.,** 2002. Preparation and Characterization of TiN–Ag Nanocomposite Films, *Vacuum*, **67**, 463-470.

[11] **Miyoshi, K.,** 2001. Durability Evaluation of Selected Solid Lubricating Films, *Wear*, **250**, 1061-1067.

[12] **Gulbinski, W., Suszko, T., Sienicki, W., Warcholinski, B.,** 2003. Tribological Properties of Silver- and Copper-Doped Transition Metal Oxide Coatings, *Wear*, **254**, 129-135.

[13] **Sung, M. S., Sung, M.,** 1996. Carbon Nitride and Other Speculative Superhard Materials, *Materials Chemistry and Physics*, **43**, 1-18.

[14] **Veprek, S.,**1995. Plasma Chemical-Vapor-Deposition and Properties of Hard C_3N_4 Thin-Films, *Journal of Vacuum Science and Technology*, **A13**, 2914-2919.

[15] **Kayalı, E. S., Çimenoğlu H.,** 1986. Malzemelerin Yapısı ve Mekanik Davranışları, ITU Kimya Metalurji Fakultesi Ofset Atölyesi, Istanbul.

[16] **Teng, Z., Teng F. and Wang Y.,** 1995. Some Applications of the Hall-Petch Relationship for Single-Phase Imperfect Polycrystals, *Materials Characterization*, **34**, 237-240.

[17] **Yashar, P.C., Sproul, W.D.,** 1999. Nanometer Scale Multilayered Hard Coatings, *Vacuum*, **55**, 179-190

[18] **Musil, J., Vlcek, J.,** 2001. Magnetron Sputtering of Hard Nanocomposite Coatings and Their Properties, *Surface and Coatings Technology*, **142-144**, 557-566.

[19] **Rebouata, L., Tavares, C. J., Aimo, R., Wang, Z., Pischow, K., Alves, E., Rojas, T. C., Odriozala J.A.,** 2000. Hard Nanocomposite Ti-Si-N Coatings Prepared by DC Reactive Magnetron Sputtering, *Surface and Coatings Technology*, **133-134**, 234-239.

[20] **Veprek, S., Nesladek, P., Niederhofer, A., Glatz, F., Jilek, M., Sima, M.,** 1998. Recent Progress in the Superhard Nanocrystaline Composites: Towards Their Industrialization and Understanding of The Origin of the Superhardness, *Surface and Coatings Technology*, **108-109**, 138-147.

[21] **Veprek, S., Reiprich, S.,** 1995. A Concept for the Design of Novel Superhard Coatings, *Thin Solid Films*, **268**, 64-71.

[22] **Bush, M.B., Kim, H.S.,** 1999. On The Modelling of Ultra-Fine Grained Materials, *Journal of Metastable and Nanocrystaline Materials*, **2-6**, 437-442.

[23] **Mitterer, C., Mayrhofer, P.H., Beschliesser, M., Losbichler P., Warbichler, P., Hofer, F., Gibson, P.N., Gissler, W., Hruby, H., Musil, J., Vlcek, V.,** 1999. Microstructure and Properties of Nanocomposite Ti-B-N and Ti-B-C Coatings, *Surface and Coatings Technology*, **120-121**, 405-411.

[24] **Veprek, S.,** 2000. Ultra Hard Nanocomposite Coatings With Hardness of 80 to 105 GPa, *Int. Cinf. On Trends and Appl. Of Thin Films, TAFT 2000, Nancy France, Societe Francaise du Vide*, Paris March, **2000**, 185-195.

[25] **Shah, S., Chokshi A.H.,** 1998. The Significance of Diffusional Flow in Ultrafine-grained Materials, *Colloids and Surfaces*, **133**, 57-61.

[26] **Arzt, E.,** 1998. Size Effects in Materials Due to Mictrostructural and Dimensional Constraints: A Comparative Review, *Acta Materialia*, **46**, 5611-5626.

[27] **Hertzberg, R.W.,** 1989. *Deformation and Fracture Mechanics of Engineering Materials*, 3rd ed., Willey, New York.

[28] **Hirth, J.P., Lothe.J.,** 1982. *Theory of Dislocations*, John Wiley & Sons, New York, second edition.

[29] **Kelly, P.J., Arnell, R.D.,** 2000. Magnetron Sputtering: A Review of Recent Developments and Applications, *Vacuum*, **56**, 159-172

[30] **Musil, J., Vlcek, J.,** 1998. Magnetron Sputtering of Films with Controlled Texture and Grain Size, *Materials Chemistry and Physics*, **54**, 116-122.

[31] **Musil, J., Vlcek, J.,** 1999. Magnetron Sputtering of Alloy and Alloy-Based Films, *Thin Solid Films*, **343-344**, 47-50.

[32] **Barna, P.B. and Adamik, M.**, 1997. Formation and Characterization of The Structure of Surface Coatings, in: *Protective Coatings and Thin Films, Synthesis, Characterization and Applications*, Eds. Pauleau, Y & Barna P.B., NATO ASI Series, Kluwer Academic Publishers, Netherlands.

[33] **Wu, J.D., Wu, C.Z. , Song, Z.M., Wu, L.H., Li, F.M.,** 1995. Synthesis of Molybdenum Nitride γ-Mo_2N by Multipulse Laser Irradiation of Molybdenum in Nitrogen, *Applied Surface Science*, **90**, 81-87

[34] **Pierson, H.O.,** 1996. *Handbook of Refractory Carbides and Nitrides*, Noyes Publications, Westwood, New Jersey.

[35] **Massalski, T.B.,** 1990. *Binary Alloys Phase Diagrams*, Materials Park, Ohio: ASM International.

[36] **Joint Committee on Powder Diffraction Standards,** 1994. *Powder Diffraction File*, International Center for Diffraction Data, Park Lane.

[37] **Anitha, V.P., Major, S., Chandrashekharam, D. and Bhatnagar, M.**, 1996. Deposition of Molybdenum Nitride Thin Films by r.f. Reactive Magnetron Sputtering, *Surface and Coatings Technology*, **79**, 50-54.

[38] **Fuller, W.W., Wolf, S.A., Gubser, D.C., Skelton, E.F. and Francavilla, T.L.,** 1983. Properties of New Molybdenum Nitrogen Phase, *Journal of Vacuum Science and Technology*, **A1**, 517-519.

[39] **Roberson, S.L., Finello, D., Davis, R.F.,** 1998. Synthesis of Low Oxygen Concentration Molybdenum Nitride Coatings, *Materials Science and Engineering*, **A248**, 198-205

[40] **Chuang, J-C., Tu, S-L., Chen, M-C.,** 1999. Sputter Deposited Mo and Reactively Sputter Deposited Mo-N Films as Barrier Layers Against Cu Diffusion, *Thin Solid Films*, **346**, 299-306.

[41] **Shih, K.K. and Dove, D.B.,** 1990. Properties of W-N and Mo-N Films Prepared by Reactive Sputtering, *Journal of Vacuum Science and Technology,* **A8**, 1359-1363.

[42] **Lin, K.L., Ho, Y.J.,** 1995. Deposition and Properties of Mo-N Films, *Journal of Vacuum Science and Technology,* **A13**, 2872-2876.

[43] **Sikola, T., Spousta, J., Ceska, R., Zlamal, J., Dittrichova, L.,** 1998. Deposition of Metal Nitrides by IBAD, *Surface and Coatings Technology*, **108-109**, 284-291

[44] **Zdanowski, J., Kozlowski, J., Markowski, J., Prajzner, A.,** 1998. Properties of Carbides, Nitrides and Carbonitrides Based on Ti and Mo Multicomponent Layers, *Surface and Coatings Technology*, **98**, 1440-1443.

[45] **Roberson, S.L., Finello, D., Davis, R.F.,** 1998. Phase Control of Mo_xN Films by Chemical Vapor Deposition, *Thin Solid Films*, **324**, 30-36.

[46] **Maoujoud, M., Offergeld, J., Bouillon, F.,** 1993. Synthesis and Characterization of Thin Film Molybdenum Nitrides, *Applied Surface Science*, **64**, 81-89.

[47] **Lee, K.H., Takai, O., Lee, M.H.,** 2003. Tribological and Corrosive Properties of Silver Thin Films Prepared by e-Beam Ion Plating Method, *Surface and Coatings Technology*, **169-170**, 695-698.

[48] **Endrino, J.L., Nainaparampil, J.J., Krzanowskia, J.E.,** 2002. Microstructure and Vacuum Tribology of TiC–Ag Composite Coatings Deposited by Magnetron Sputtered-Pulsed Laser Deposition, *Surface and Coatings Technology*, **157**, 95-101.

[49] **Perry's Chemical Engineers' Handbook**, 1997. McGraw-Hill, New York.

[50] **Bhushan, B.,** 1999. *Principles and Applications of Tribology*, Wiley-Interscience, New York.

[51] **Rabinowicz, E.,** 1965. *Friction and Wear of Materials*, Wiley, New York.

[52] **Bowden, F.P.,** 1954. *The Friction and Lubrication of Solids*, Claderon Press, Oxford.

[53] **Blau, P.J.,** 1999. *Friction Sciene and Technology*, Marcel Dekker, New York.

[54] **Stachowiak, G.W., Batchelor, A.W.,** 2000. *Engineering Tribology*, Butterworth-Heinemann, Boston.

[55] **ASM Handbook,** 1995. Friction, Lubrication and Wear Technology, 2nd Printing, Vol.18, ASM International, Materials Park, Ohio.

[56] **Bhushan, B., Gupta, B.K.,** 1997. *Handbook of Tribology*, Krieger Pub., Malabar, Fla.

[57] **Wulpi, D.J.,** 1985. *Understanding How Components Fail*, ASM, Metals Park, Ohio.

[58] **Osma, A.,** 1999. İnce Sert Seramik Kaplamaların Kazımalı Aşınma Davranışları ile Endüstriyel Zımbalama İşlemine Uygulanmaları, *Doktora Tezi*, İ.T.Ü. Fen Bilimleri Enstitüsü, İstanbul.

[59] **Hutchings, I.M.,** 1992. *Tribology: Friction and Wear of Engineering Materials*, Edward Arnold, London.

[60] **Anonymous**, 2002. *CSM: Spherical Abbrasion Test*, http://www.csm-instruments.com/frames/princ_spher.html.

[61] **He, J.L., Setsuhara, Y., Shimizu , I., Miyake, S.,** 2001. Structure Refinement and Hardness Enhancement of Titanium Nitride Films by Addition of Copper, *Surface and Coatings Technology*, **137**, 38-42.

[62] **Zeman, P., Cerstvy, R., Mayrhofer, P.H., Mitterer, C., Musil, J.,** 2000, Structure and Properties of Hard and Superhard Zr-Cu-N Nanocomposite Coatings, *Materials Science and Engineering*, **A289**, 189-197.

[63] **Musil, J., Leipner, I., Kolega, M.,** 1999. Nanocrystalline and Nanocomposite CrCu and CrCu-N Films Prepared by Magnetron Sputtering, *Surface and Coatings Technology*, **115**, 32-37.

[64] **Musil, J., Zeman, P., Hruby, H., Mayrhofer, P.H.,** 1999, ZrN/Cu Nanocomposite Film – A Novel Superhard Material, *Surface and Coatings Technology*, **120-121**, 179-183.

RESUME

Tuncay TURUTOĞLU was born in Istanbul in 1979. After finishing Sefaköy High Scholl in 1995, he started Istanbul Technical University, Metallurgical and Materials Engineering Department in 1996. He graduated from Istanbul Technical University in 2001, as a Metallurgical and Materials Engineer. In the same year he participated M. Sc. Program in Materials Science and Engineering Department at Istanbul Technical University.